Spring 2011

Building and deployment of an automated, in situ greenhouse gas gas chromatographic system

Andrew H. Hart
University of New Hampshire, Durham

BUILDING AND DEPLOYMENT OF AN AUTOMATED, IN SITU GREENHOUSE GAS GAS CHROMATOGRAPHIC SYSTEM

BY

ANDREW H. HART

B.S., Chemistry, University of New Hampshire, 2009

THESIS

Submitted to the University of New Hampshire

in Partial Fulfillment of

the Requirements for the Degree of

Master of Science

In

Chemistry

May, 2011

This thesis has been examined and approved.

Barkley C. Sive, Research Associate Professor,
Climate Change Research Center

Howard R. Mayne, Professor, Chemistry
Department

Edward H. Wong, Professor, Chemistry
Department

5/6/2011

Date

ACKNOWLEDGMENTS

I would like to express my sincere gratitude to my advisors Dr. Barkley Sive and Dr. Howard Mayne for the continuous support during this research, for their patience, insights and motivation. I would also like to thank Dr. Edward Wong of my thesis committee and the VOC group for their encouragement and insightful comments.

I also thank my family and friends for their support and encouragement of all my endeavors.

Financial support for this work was provided through the Office of Oceanic and Atmospheric Research at the National Oceanic and Atmospheric Administration as part of AIRMAP. Additional support was provided through the University of New Hampshire Chemistry Department.

TABLE OF CONTENTS

LIST OF FIGURES

LIST OF TABLES

Page

LIST OF EQUATIONS

Page

LIST OF REACTIONS

ABSTRACT

BUILDING AND DEPLOYMENT OF AN AUTOMATED, IN SITU GREENHOUSE GAS GAS CHROMATOGRAPHIC SYSTEM

by

Andrew H. Hart

University of New Hampshire, May, 2011

High-precision, continuous monitoring of greenhouse gases, such as carbon dioxide (CO_2), methane (CH_4), nitrous oxide (N_2O), sulfur hexafluoride (SF_6), and the criteria pollutant carbon monoxide (CO), is important for characterizing their regional sources and sinks and understanding how their ambient levels are changing with time and associated anthropogenic activities. For monitoring this suite of gases, a fully automated gas chromatographic based analytical system was built and deployed in the field at the UNH AIRMAP Observing Station at Thompson Farm in Durham, NH. The instrument consists of a Shimadzu 17A gas chromatograph (GC), equipped with a Flame Ionization Detector and a custom built methanizer for the measurements of CO_2, CH_4 and CO; additionally, the GC is equipped with an Electron Capture Detector for measurements of N_2O and SF_6. Results from the ambient analyses of this suite of gases provide confidence in the methanizer efficiency, calibration standards and the system's overall performance.

CHAPTER 1

GREENHOUSE GASES

1.1. Introduction

The Earth's climate is dependent upon the radiative balance of the atmosphere. Therefore any deviation from the natural balance of incoming solar radiation (short wavelengths predominately in the visible or ultraviolet) and outgoing energy flux (longer wavelengths primarily in the infrared) from the Earth would result in heating or cooling [*Berner and Berner*, 1996; *Watson et al.*, 1990]. Furthermore, Earth's climate is also dependent on the atmospheric abundances of radiatively active trace gases, clouds and aerosols [*Watson et al.*, 1990].

The main focus of this work is on monitoring the atmospheric abundances of the radiatively active trace gases, i.e., greenhouse gases (GHGs). These include carbon dioxide (CO_2), methane (CH_4), nitrous oxide (N_2O) and sulfur hexafluoride (SF_6) and the trace gas carbon monoxide (CO). This suite of GHGs absorbs thermal radiation, corresponding to vibrational and vibrational-rotational transitions, in the wavelength range of 5-50 μm [*Jacob*, 1999]. Figure 1 shows the wavelength range of maximum emissions from Earth's surface (5-20 μm) and the corresponding major atmospheric absorbers of terrestrial radiation in the Earth's atmosphere.

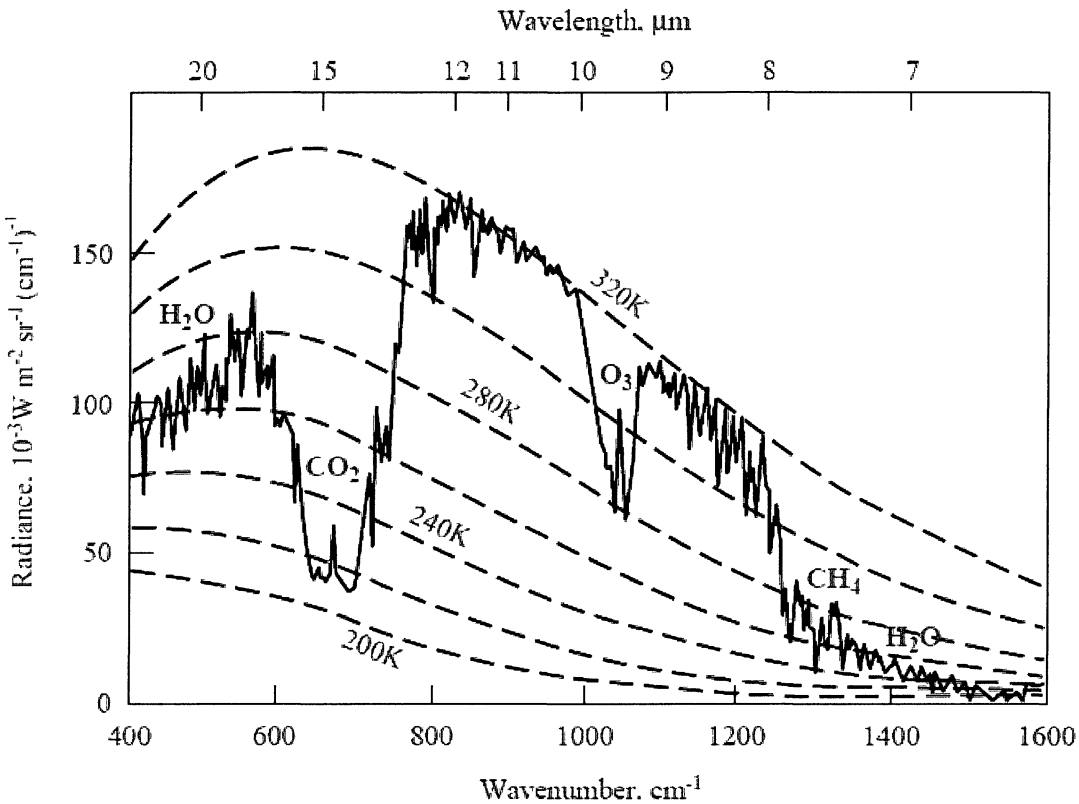

Figure 1. Terrestrial radiation spectrum measured from a satellite over northern Africa with the major atmospheric absorbers identified [*Jacob*, 1999].

The thermal radiation absorbed by CO_2, CH_4, N_2O and SF_6 is then reradiated back to Earth [*Forster et al.*, 2007]. This is known as the "greenhouse effect" and it has been a growing concern as it is evident that the chemical composition of the Earth's atmosphere is changing, largely due to human activities [*Watson et al.*, 1990]. Although the greenhouse effect is a naturally occurring phenomenon in the atmosphere, human activities have contributed to increased concentrations of GHGs which ultimately amplifies the process [*Forster et al.*, 2007]. Table 1 provides the magnitude of this change for the select greenhouse gases. It is apparent that abundance of each of the gases has increased significantly since the pre-industrial times (AD 1000-1750).

Table 1. Global atmospheric mixing ratios, atmospheric lifetimes and global warming potentials (GWP) over 100 years time period of CO_2, CH_4, N_2O and SF_6.

Atmospheric Species	Pre-industrial Mixing Ratio (IPCC 2001)	Mixing Ratio in 2005 (IPCC 2007)	Atmospheric lifetime (years) (IPCC 2001)	GWP – 100 years (IPCC 2007)
CO_2	278 ppmv	379 ± 0.65 ppmv	50-200	1
CH_4	715 ppbv	1,774 ± 1.8 ppbv	12	25
N_2O	270 ppbv	319 ± 0.12 ppbv	114	298
SF_6	0 pptv	5.6 ± 0.038 pptv	3,200	22,800

Each of these atmospheric species has a different influence in altering the balance of incoming and outgoing energy in the Earth's atmosphere. A measure of these influences is described in terms of radiative forcing, which quantitatively compares the different strengths of factors that ultimately result in climate change [*Forster et al.*, 2007]. Radiative forcing is the net flux at the tropopause, in watts per square meter (Wm^{-2}), corresponding to a concentration change of each particular gas [*Ramaswamy et al.*, 2001]. Figure 2 shows that the three most important long-lived greenhouse gases (LLGHGs) (CO_2, CH_4 and N_2O) all have a positive radiative forcing, which is indicative of a warming effect on the Earth's surface.

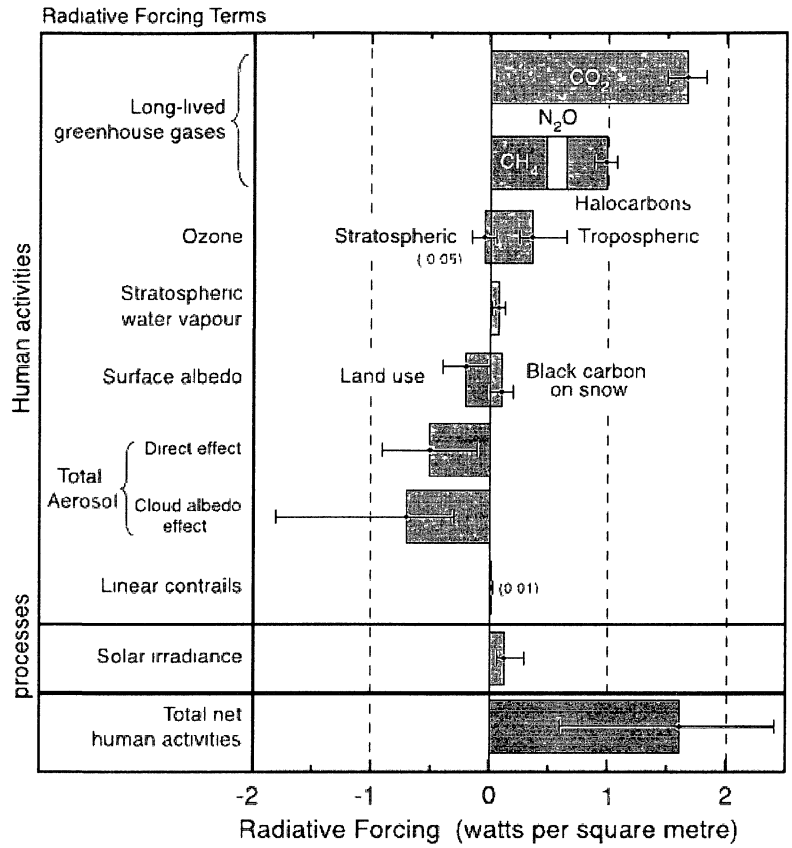

Figure 2. Global mean radiative forcing resulting from changes in greenhouse gas concentrations, aerosols and solar activity from 1750 to 2005 [*Forster*, 2007].

Although radiative forcing is useful in comparing the different strengths of factors that influence climate change, it cannot be used independently to evaluate the potential climate change related to emissions [*Forster*, 2007]. This is because it does not take into account the different atmospheric lifetimes of these gases (i.e., the time required to turn over the global atmospheric burden for each gas [*Ramaswamy et al.*, 2001]). Thus, Global Warming Potentials (GWPs) are used, which are a quantified measure of the globally averaged relative radiative forcing impacts of a particular greenhouse gas [*U.S. EPA*, 2010]. Table 1 provides the GWPs for the GHGs of interest over a 100 year time period. CO_2 has a GWP of 1, as it is used as a reference gas and SF_6 has a GWP of 22,800, making it the most potent GHG. These GWPs are further used to calculate a

weighted emission of a GHG, which is measured in teragrams of CO_2 equivalent (Tg CO_2 Eq.). The corresponding equation for the weighted emission is expressed in Equation 1,

$$Tg\,CO_2\,Eq. = (Gg\ of\ gas)(GWP)\left(\frac{Tg}{1{,}000\,Gg}\right) \quad (1)$$

where Tg CO_2 Eq. is teragrams of CO_2 equivalent, Gg is gigagrams, GWP is the Global Warming Potential of a given gas and Tg is teragrams [*U.S. EPA*, 2010]. The emissions of the suite of GHGs in this report are reported in terms of Tg CO_2 Eq. in the subsequent sections.

1.1.1. Atmospheric Carbon Dioxide (CO_2)

Carbon Dioxide is the most important greenhouse gas in terms of radiative forcing (RF) (Figure 2). Atmospheric mixing ratios of CO_2 have increased from about 278 parts per million by volume (ppmv) during the pre-industrial times to 379 ± 0.65 ppmv in 2005 (Table 1) [*U.S. EPA*, 2010]. This observed increase is a direct result of the use of fossil fuel in transportation, building heating and cooling and the manufacture of cement and other goods. Deforestation also releases CO_2 and reduces its uptake by plants [*Forster*, 2007]. Table 2 provides an extensive description of the current (2008) anthropogenic sources of CO_2 emissions and their relative magnitudes. It is apparent that the predominant source of anthropogenic CO_2 emissions is the combustion of fossil fuels, which accounts for 5,572.8 Tg CO_2 Eq. out of the total 5,921.1 Tg CO_2 Eq.

Table 2. U.S. Atmospheric CO_2 (Tg CO_2 Eq.) emissions in 2008 [*U.S. EPA*, 2010]. The result in bold represents the total emissions.

CO_2	**5,921.2**
Fossil Fuel Combustion	5,572.8
Electricity Generation	2,363.5
Transportation	1,785.3
Industrial	819.3
Residential	342.7
Commercial	219.5
U.S. Territories	42.5
Non-Energy Use of Fuels	134.2
Iron and Steel Production & Metallurgical Coke Production	69.0
Cement Production	41.1
Natural Gas Systems	30.0
Lime Production	14.3
Incineration of Waste	13.1
Ammonia Production and Urea Consumption	11.8
Cropland Remaining Cropland	7.6
Limestone and Dolomite Use	6.6
Aluminum Production	4.5
Soda Ash Production and Consumption	4.1
Petrochemical Production	3.4
Titanium Dioxide Production	1.8
Carbon Dioxide Consumption	1.8
Ferroalloy Production	1.6
Phosphoric Acid Production	1.2
Wetlands Remaining Wetlands	0.9
Petroleum Systems	0.5
Zinc Production	0.4
Lead Production	0.3
Silicon Carbide Production and Consumption	0.2

CO_2 is primarily taken up by the land biosphere and ocean in comparable magnitudes [*Popa*, 2008]. C.D. Keeling, from the Scripps Institution of Oceanography, is well recognized for his contributions in the continuous *in situ* high-precision measurements of atmospheric CO_2 since 1958 (Mauna Loa, Hawaii) [*Scripps CO_2 Program*, 2010]. This long term data set is now infamously known as the "Keeling curve" (Figure 3). The acquired data not only revealed that CO_2 was increasing in the atmosphere but it also led to an understanding of the observed terrestrial biological cycling [*Forster et al.*, 2007].

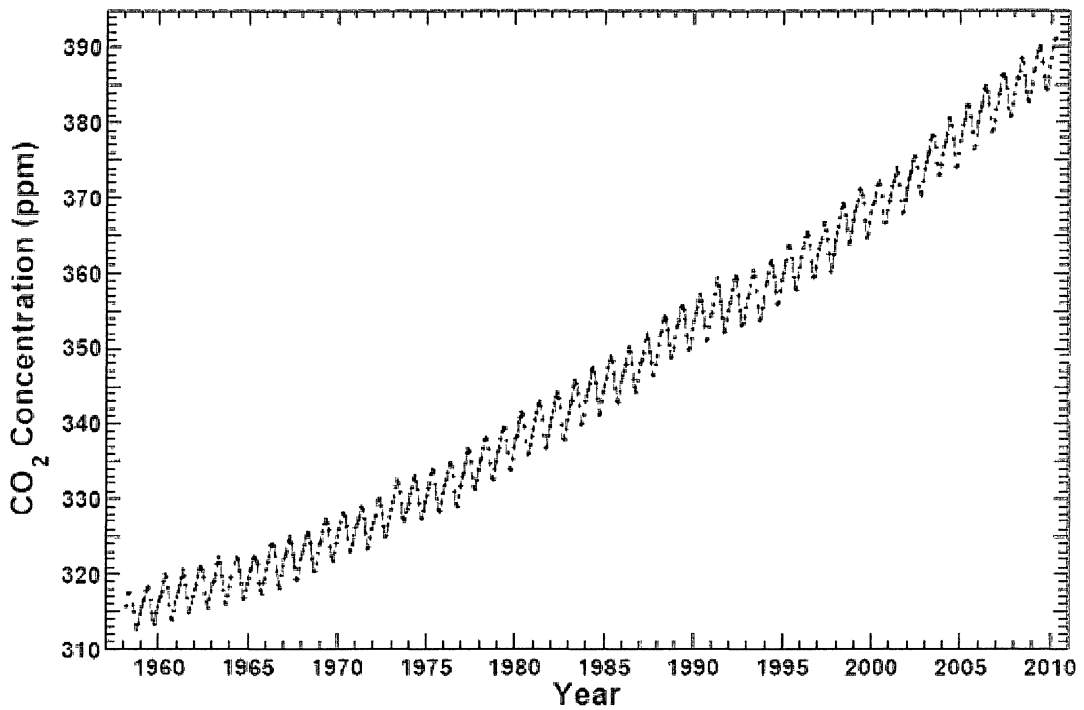

Figure 3. Mean monthly concentration of atmospheric CO_2 (ppm) as a function of time at Mauna Loa Observatory, Hawaii from 1958-2010 [Scripps CO_2 Program, 2010].

This observed cycling in the atmospheric concentration of CO_2 is closely related to the biogeochemical carbon cycle which involves the exchange of carbon with the terrestrial biosphere, the ocean and the marine biosphere [*Popa*, 2008]. Moreover, a decrease in concentration is a result of photosynthesis, i.e., uptake of CO_2, and an increase in concentration is because of respiration, i.e., release of CO_2 [*Berner and Berner*, 1996]. A three-dimensional (3-D) representation of the global distribution of CO_2 in the remote marine boundary layer is shown in Figure 4.

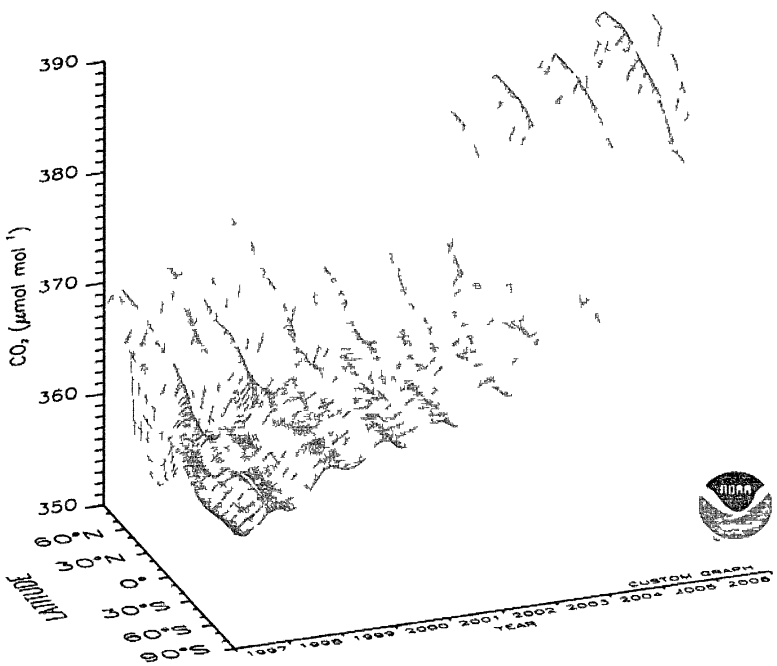

Figure 4. Global distribution of CO_2 in the remote marine boundary layer from 1997-2006 [*Tans, 2010*]

Figure 4 illustrates the seasonality and latitudinal gradient for atmospheric carbon dioxide The difference in both amplitude and phase of the seasonal variation in CO_2 mixing ratios is shown in both hemispheres. The existing seasonality is primarily the result of the seasonal imbalance between photosynthesis and respiration of land plants [*Conway et al*, 1988] Furthermore, the latitudinal variation of the atmospheric CO_2 concentration signifies larger sources and sinks in the Northern Hemisphere, than the Southern Hemisphere [*Conway et al*, 1988].

1.1.2. Atmospheric Methane (CH_4)

Methane has the second-largest RF of the LLGHGs after CO_2 [*Forster et al*, 2007] Atmospheric mixing ratios of CH_4 have increased from about 715 parts per billion by volume (ppbv), in the pre-industrial times, to 1,774 ± 1.8 ppbv in 2005 (Table 1). The sources of CH_4 are mostly biogenic, as it is primarily produced through anaerobic

decomposition of organic matter and include wetlands, rice agriculture, biomass burning and ruminant animals [*Forster et al.*, 2007; *U.S. EPA*, 2010]. Anthropogenic sources of methane arise from industrial processes including fossil fuel mining and its distribution [*Forster et al.*, 2007]. Table 3 provides an extensive description of the current (2008) anthropogenic sources of CH_4 emissions and their relative magnitudes.

Table 3. U.S. Atmospheric CH_4 (Tg CO_2 Eq.) Emissions in 2008 [*U.S. EPA*, 2010]. The result in bold represents the total emissions.

CH_4	**567.6**
Enteric Fermentation	140.8
Landfills	126.3
Natural Gas Systems	96.4
Coal Mining	67.6
Manure Management	45.0
Petroleum Systems	29.1
Wastewater Treatment	24.3
Forest Land Remaining Forest Land	11.9
Rice Cultivation	7.2
Stationary Combustion	6.7
Abandoned Underground Coal Mines	5.9
Mobile Combustion	2.0
Composting	1.7
Field Burning of Agricultural Residues	1.0
Petrochemical Production	0.9
Iron and Steel Production & Metallurgical Coke Production	0.6

The primary removal mechanism for CH_4 is through a reaction with the hydroxyl radical (OH), in which CH_4 is converted to CO_2 [*Brasseur et al.*, 1999; *U.S. EPA*, 2010]. A 3-D representation of the global distribution of CH_4 in the remote marine boundary layer is shown in Figure 5.

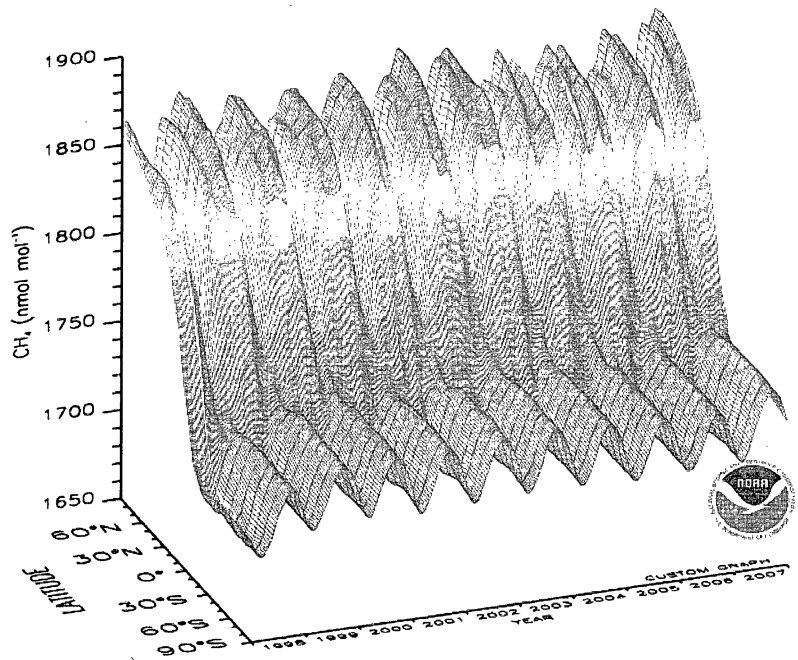

Figure 5. Global distribution of CH_4 in the remote marine boundary layer from 1998-2007 [*Tans, 2010*].

Figure 5 illustrates the seasonality and latitudinal gradient for atmospheric methane. The seasonal variation in CH_4 mixing ratios appear to be opposite in phase in both hemispheres, with a minimum occurring in summer and maximum in winter or spring [*Dlugokencky et al.*, 1997]. The seasonal cycle in the Northern Hemisphere results from seasonal variations in sources, sinks and atmospheric transport. For example, CH_4 emissions from sources such as wetlands and biomass burning vary with changes in soil moisture content and temperature, and with wet and dry seasons, respectively [*Dlugokencky et al.*, 1997]. In the Southern Hemisphere the variation is mostly driven by chemical destruction as the major source regions for atmospheric methane reside in the Northern Hemisphere [*Dlugokencky et al.*, 1994; *Dlugokencky et al.*, 1997; *Steele et al.*, 1987]. Furthermore, the absence of significant sources of methane in the Southern Hemisphere yields the latitudinal gradient in which higher concentrations of methane are observed in the Northern Hemisphere.

1.1.3. Atmospheric Nitrous Oxide (N_2O)

Nitrous oxide is a long-lived trace constituent of the atmosphere having a lifetime of 114 years [*Ramaswamy et al.*, 2001]. Atmospheric mixing ratios of N_2O have increased from about 270 ppbv during the pre-industrial times, to 319 ppbv in 2005 (Table 1). Anthropogenic emissions of N_2O consist of biomass burning, fossil fuel combustion, industrial production of adipic (used in nylon production) and nitric acids, and the use of nitrogen fertilizer. Biogenic sources include chemical oxidation of ammonia in the atmosphere, microbes and bacteria [*U.S. EPA*, 2010; *Popa*, 2008]. Table 4 provides an extensive description of the current (2008) anthropogenic sources of N_2O emissions and their relative magnitudes.

Table 4. U.S. Atmospheric N_2O (Tg CO_2 Eq.) Emissions in 2008 [*U.S. EPA*, 2010]. The result in bold represents the total emissions.

N_2O	**318.2**
Agricultural Soil Management	215.9
Mobile Combustion	26.1
Nitric Acid Production	19.0
Manure Management	17.1
Stationary Combustion	14.2
Forest Land Remaining Forest Land	10.1
Wastewater Treatment	4.9
N_2O from Product Uses	4.4
Adipic Acid Production	2.0
Composting	1.8
Settlements Remaining Settlements	1.6
Field Burning of Agricultural Residues	0.5
Incineration of Waste	0.4

The primary removal mechanisms for N_2O are by photolysis and reaction with electronically excited oxygen atoms e.g., $O(^1D)$ [*Popa*, 2008]. A 3-D representation of the global distribution of N_2O in the remote marine boundary layer is shown in Figure 6.

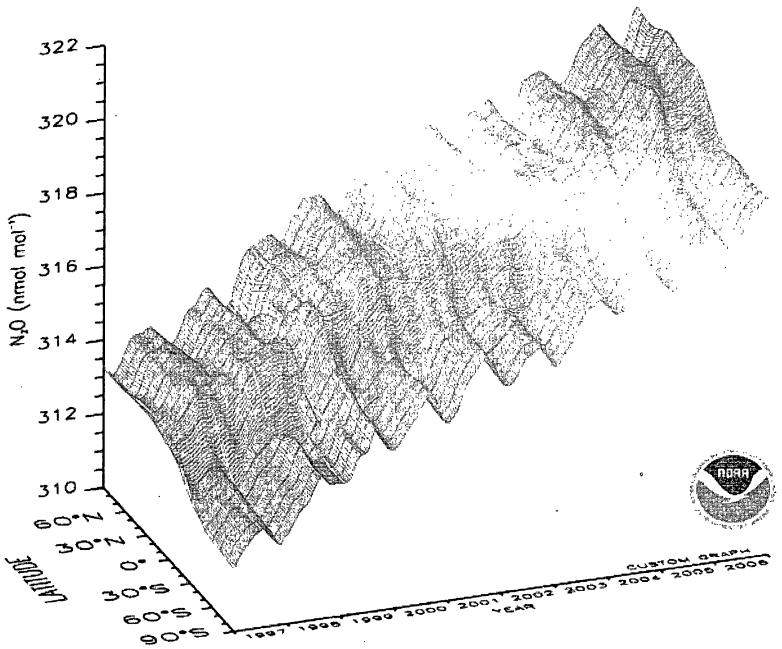

Figure 6. Global distribution of N_2O in the remote marine boundary layer from 1997-2006 [*Tans, 2010*].

Figure 6 illustrates the seasonality and increasing concentration of atmospheric nitrous oxide. The seasonal variation in N_2O mixing ratios shows there is a minimum occurring in summer, which is generally attributed to tropospheric transport processes, e.g., interhemispheric exchange [*Nevison, Kinnison and Weiss*, 2004]. There is also some speculation of stratospheric influence on the observed minimum in summer [*Nevison, Kinnison and Weiss*, 2004]. The growth in atmospheric N_2O is mainly attributed to an increase in anthropogenic sources, e.g., biomass burning, agricultural activities and industrial sources [*Tohjima et al.*, 2000].

1.1.4. Atmospheric Sulfur Hexafluoride (SF_6)

Sulfur hexafluoride is the most potent greenhouse gas the IPCC has evaluated [*U.S. EPA*, 2010]. It is extremely long-lived (3,200 years) and has a global warming potential 22,800 times that of CO_2 over a 100 year period (Table 1). Atmospheric mixing ratios of SF_6 have increased from about 0 parts per trillion by volume (pptv) in the pre-

industrial times to 5.6 ± 0.038 pptv in 2005 (Table 1). SF_6 is predominately emitted from industrial processes including the electrical industry where it is used as a dielectric medium for high voltage equipment, the semiconductor industry and the magnesium and aluminum industry [*Popa*, 2008]. The relative magnitudes of these anthropogenic sources are provided in Table 5.

Table 5. U.S. Atmospheric SF_6 (Tg CO_2 Eq.) Emissions in 2008 [*U.S. EPA*, 2010]. The result in bold represents the total emissions.

SF_6	**16.1**
Electrical Transmission and Distribution	13.1
Magnesium Production and Processing	2.0
Semiconductor Manufacturing	1.1

SF_6 is also released into the atmosphere through its use as an inert tracer to study atmospheric and oceanic transport [*Popa*, 2008]. A 3-D representation of the global distribution of SF_6 in the remote marine boundary layer is shown in Figure 7. Figure 7 further illustrates the considerable increase in concentration of atmospheric SF_6 and the absence of any significant seasonal variation in SF_6 emissions [*Patra et al.*, 2009]. Lastly, SF_6 decreases slightly from high latitudes toward the equator in the Northern Hemisphere and appears moderately well mixed in the Southern Hemisphere, a phenomenon consistent with high emission rates of anthropogenic origin [*Geller et al.*, 1997].

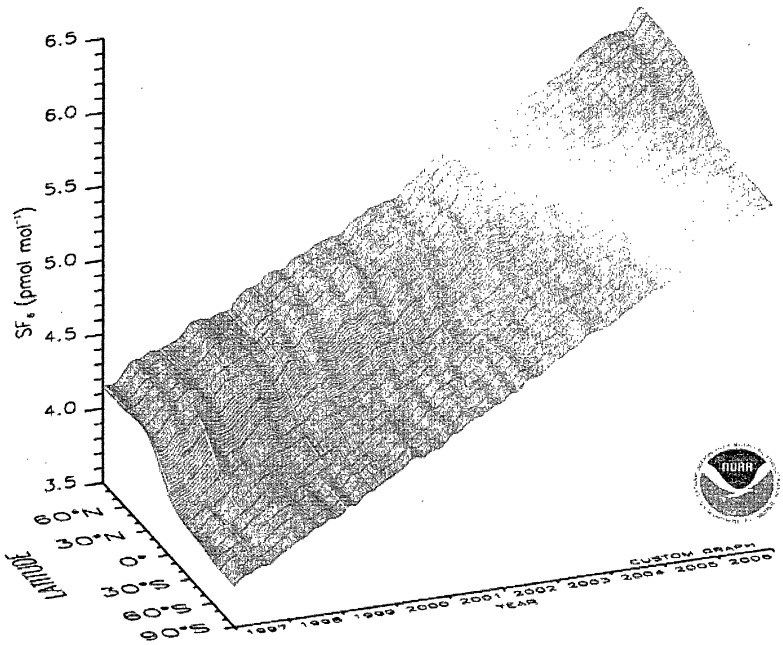

Figure 7. Global distribution of SF_6 in the remote marine boundary layer from 1997-2006 [*Tans, 2010*].

1.1.5. Atmospheric Carbon Monoxide (CO)

Carbon monoxide is a short-lived (2-3 months) trace gas in the atmosphere that is considered to be an indirect greenhouse gas [*Watson et al.*, 1990]. It has the most significant influence on the abundance of OH in the troposphere, where its reaction yields the oxidation of CO to CO_2 [*Popa*, 2008; *Brasseur et al.*, 1999] as shown in Reaction 1.

$$OH + CO \rightarrow H + CO_2 \quad (1)$$

This reaction ultimately affects the oxidative capacity of the troposphere, thus explaining the indirect radiative forcing effect of CO, as OH would otherwise be removing gases such as CH_4 in the atmosphere [*Popa*, 2008; *Brasseur et al.*, 1999]. CO is also considered to be a precursor of tropospheric ozone (O_3) as its oxidation contributes to O_3 production when there is sufficient nitric oxide (NO) available [*Mao and Talbot*, 2004; *Brasseur et al.*, 1999]. Moreover, CO emissions have the capability of contributing, directly and/or

indirectly, to the overall increase in three radiatively active trace gases (e.g., CO_2, CH_4 and O_3) in the atmosphere.

CO is a criteria pollutant (i.e., a pollutant that is commonly found throughout the United States and therefore used as an indicator of air quality), regulated by the Environmental Protection Agency (EPA), as it can cause detrimental human health effects by reducing oxygen delivery to the body's organs [www.epa.gov]. Direct anthropogenic sources of CO arise when carbon-containing fuels undergo incomplete combustion, e.g., fossil fuel combustion [*U.S. EPA*, 2010]. Table 6 provides an extensive description of the current (2008) anthropogenic sources of CO_2 emissions and their relative magnitudes. Atmospheric sources of CO include oxidation of natural and anthropogenic CH_4 and non-methane hydrocarbons (NMHCs) [*Watson et al.*, 1990].

Table 6. U.S. Atmospheric CO (Gg) Emissions in 2008 [*U.S. EPA*, 2010]. The result in bold represents the total emissions.

CO	**60,739**
Mobile Fossil Fuel Combustion	51,533
Stationary Fossil Fuel Combustion	4,792
Industrial Processes	1,682
Incineration of Waste	1,430
Agricultural Burning	970
Oil and Gas Activities	322
Waste	7
Solvent Use	2

1.2. Summary

It is apparent that human activities have contributed significantly to the emissions of the suite of GHGs of interest for this work; CO_2, CH_4, N_2O and SF_6. These gases have accumulated in the atmosphere resulting in increased concentrations with time [*Forster*, 2007]. Furthermore, the increasing concentrations of LLGHGs since the industrial times (Figure 8) have lead to a combined radiative forcing of +2.30 [+2.07 to +2.53] watts per meter squared (Wm^{-2}) [*Forster*, 2007].

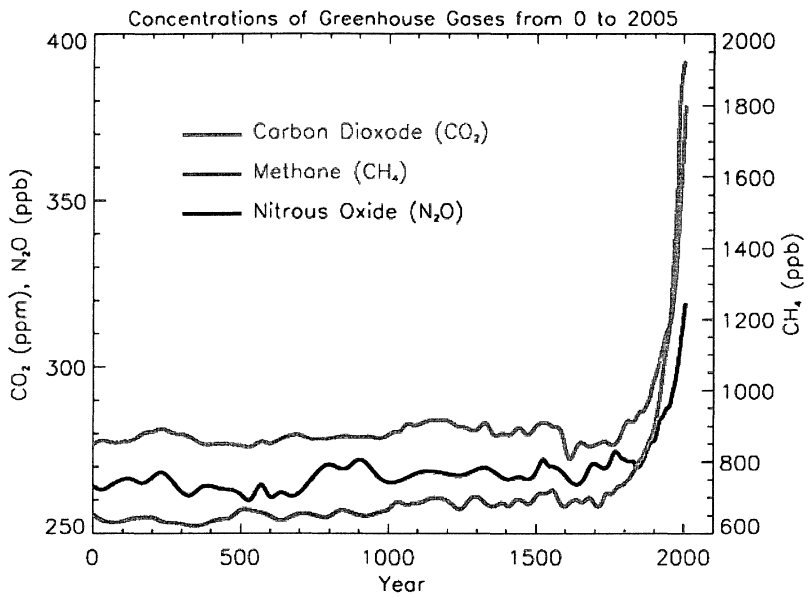

Figure 8. Increase in atmospheric concentrations of important LLGHGs due to human activities in the industrial era (~1750) [*Forster*, 2007].

Considering these facts, high-precision, continuous monitoring of the ambient mixing ratios of CO_2, CH_4, N_2O, SF_6 and CO is desired to improve our knowledge of their regional sinks and sources and to accurately establish their inter-annual variations such that we can better understand and predict how changes in ambient concentrations will perturb the balance of Earth's atmosphere [*Van der Laan*, 2009].

CHAPTER 2

INSTRUMENT DESIGN FOR MEASURING CO_2, CH_4, N_2O, SF_6 and CO

2.1. Introduction

The main driver of recent climatic changes on Earth is the increasing concentration of infrared-active gases, or greenhouse gases (GHGs) [*Kozlova and Manning*, 2009]. High-precision, continuous monitoring of GHG ambient mixing ratios is essential to improve our knowledge of their regional sources and sinks. This can help predict how these temporal changes influence the radiative balance of the atmosphere [*Van der Laan*, 2009; *Thompson et al.*, 2009]. Therefore, this work is concerned with monitoring the atmospheric abundances of the radiatively active trace gases carbon dioxide (CO_2), methane (CH_4), nitrous oxide (N_2O) and sulfur hexafluoride (SF_6) as well as the criteria pollutant carbon monoxide (CO). *In situ* analysis for this suite of gases is achieved through gas chromatographic methods employing two different detection techniques.

A Shimadzu 17A gas chromatograph (GC) was used for analysis. Both packed and capillary columns were explored for the gas-solid chromatographic (GSC) separation of the suite of compounds that were investigated. GSC is a separation technique in which

the gaseous mobile phase forces the analytes through the stationary phase, which is a solid adsorbent material. The components of the sample distribute themselves between the mobile phase and the surface of the adsorbent and those with a strong affinity to the stationary phase move slowly with the flow of the mobile phase. Compounds that are weakly adsorbed to the stationary phase travel rapidly through the column, therefore, allowing the sample components to separate and to be analyzed qualitatively or quantitatively [*Crouch et al.*, 1998; *Hart*, 2009]. Three detectors (flame ionization detector, pulsed discharge helium ionization detector, and electron capture detector) were examined for measuring the target analytes following their chromatographic separation.

2.1.1. Detectors

2.1.1.1. Flame Ionization Detector

A flame ionization detector (FID) (Figure 9) utilizes ultra-high purity (UHP) hydrogen gas with air to fuel a small air-hydrogen flame to which the effluent from the column is directed. Ions and electrons are produced when an organic compound burns in the flame resulting in a current that can be measured. A large electrical potential is applied between the burner tip and the collector electrode located above the flame. This results in a current when the ions and electrons move towards the collector. The resulting current from the pyrolysis can then be measured [*Crouch et al.*, 1998]. The current is measured in analog signals that are converted to digital signals for use in integrators or computers for quantification [*Cockerham and Shane*, 1994].

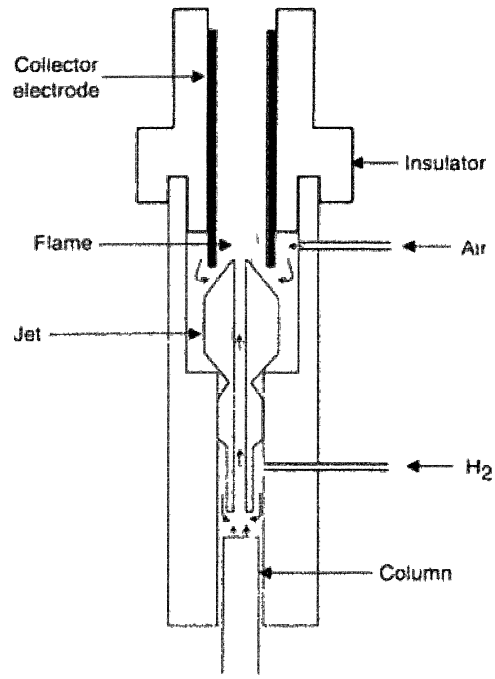

Figure 9. Schematic of a typical flame ionization detector (FID) [*Nollet*, 2006].

The FID is a mass-sensitive rather than a concentration-sensitive detector. An advantage to this is that changes in mobile phase flow rate do not affect the detector's response. The FID is also a practical detector of organic compounds; it has a high sensitivity, a large linear response range, and low noise [*Crouch et al.*, 1998]. The detector is sensitive to compounds which contain C-C or C-H bonds, but less sensitive to certain functional groups of organic compounds, such as alcohol, amine, carbonyl, and halogens, and is insensitive towards noncombustible gases (e.g., H_2O, CO_2, SO_2 and NO) [*Yuwono and Indrayanto*, 2005].

2.1.1.2. Pulsed Discharge Helium Ionization Detector

The pulsed discharge helium ionization detector (PDHID) (Figure 10) is a universal detector that utilizes a constant, low power, pulsed DC discharge in helium as its ionization source.

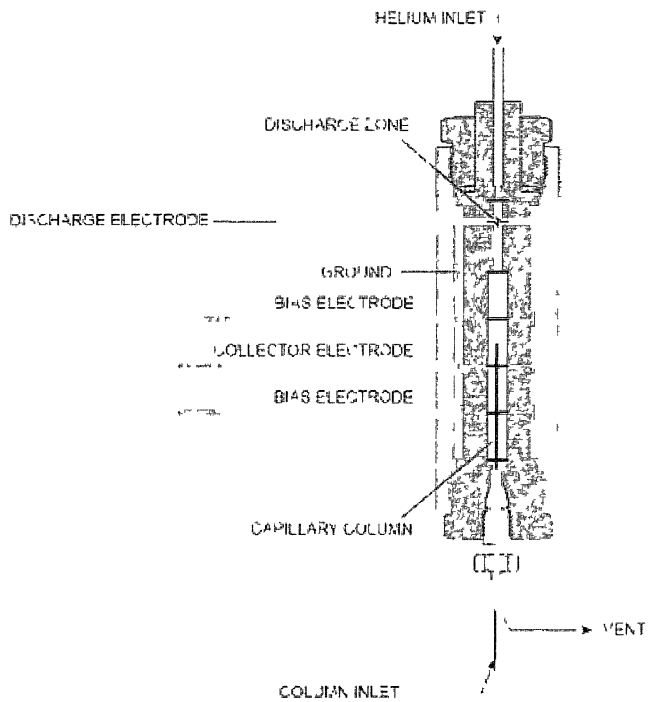

Figure 10. Schematic of a pulsed discharge helium ionization detector (PDHID) [*VICI Valco Instruments Co. Inc.*, 1998].

The PDHID operates such that compounds eluting from the column, flowing counter to the flow of helium from the discharge zone, are ionized by high-energy photons from the helium discharge zone. Electrons resulting from ionization are focused toward the collector electrode by the bias electrodes where they effectively change the measured current, i.e., the detectors response [*VICI Valco Instruments Co. Inc.*, 1998; *Forsyth*, 2004].

The principal mode of ionization is photoionization by radiation arising from the transition of excited state diatomic helium to the dissociative ground state produced in plasma,

$$He_2\left(A^1\Sigma_u\right) \rightarrow 2He\left(1^1 S_0\right)$$

This is a Hopfield emission which occurs at short wavelengths (e.g. 60-100 nm) and energies in the range of 13.5 to 17.7 eV. The resulting energy from the broad emission

can adequately ionize all elements and compounds, except neon, thus making it ideal to detect the suite of gases of interest with the GHG GC system [*VICI Valco Instruments Co. Inc.*, 1998; *Forsyth*, 2004].

2.1.1.3. Electron Capture Detector

The electron capture detector (ECD) (Figure 11) is sensitive to halogen-containing organic compounds, i.e., compounds with high electronegativity.

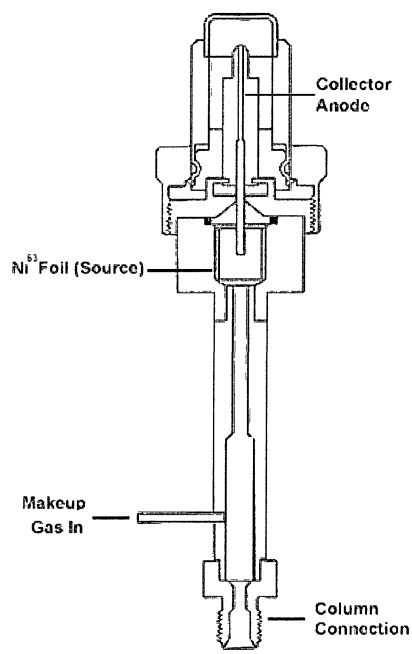

Figure 11. Typical schematic of an electron capture detector (ECD) [adapted from www.perkinelmer.com].

Effluent from the column is directed over a radioactive β emitter (^{63}Ni) [*Crouch et al.*, 1998]. Nitrogen carrier gas is ionized by the emitted electrons, resulting in a burst of electrons. The resulting constant standing current decreases significantly when an organic molecule containing electronegative functional groups passes over the ^{63}Ni, where it effectively captures electrons resulting in a decreased response.

2.1.2. Sample Air Drying System

Water vapor concentration varies considerably in atmospheric samples [e.g., *Karbiwnyk et al.*, 2002]. The presence of water in ambient air can be problematic during sampling as well as during chromatographic separation and detection. Water can significantly lower the capacity of the adsorbents in addition to causing baseline perturbations and retention time shifts in the chromatogram [*Haberhauer-Troyer, Rosenberg and Grasserbauer*, 1999]. Therefore, to ensure column stability for the desired measurements, the sample air must be dried prior to separation and subsequent detection. This is accomplished by directing samples through a Nafion membrane pre-dryer (MD-110-72P-4, Perma Pure, Toms River, New Jersey) to efficiently remove water prior to analysis and maintain a constant relative humidity.

A Nafion membrane is semi-permeable to polar compounds, especially water [*Karbiwnyk et al.*, 2002]. Nafion is an ionic polymer with a tetrafluoroethylene backbone and perfluorinated ether side chains terminating in hydrophilic sulfonic acid sites (Figure 12) [*Leckrone and Hayes*, 1997].

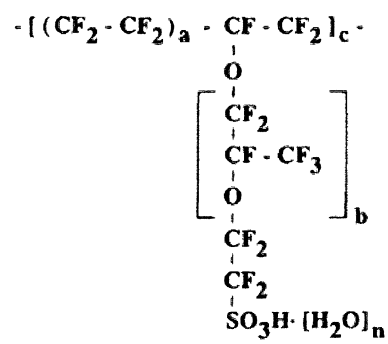

Figure 12. The chemical structure of the Nafion membrane polymer, where a = 5-11, b = 1-3, c ≈ 1000 and n = 1-13 [*Leckrone and Hayes*, 1997].

Each sulfonic acid group in the polymer can be hydrated by up to 13 water molecules, resulting in the absorption of up to 22% by weight of water [*Leckrone and Hayes*, 1997].

The Nafion membrane pre-dryer operates by using a counter-flow of dry air on the outside of the membrane, resulting in a vapor pressure gradient of water across the membrane, which drives the transfer of water from the carrier to the purge gas. Nafion dryers are found to be highly selective for water, resistant to chemical degradation and impermeable to many analytes [*Leckrone and Hayes*, 1997].

2.1.3. Methanizer for CO and CO_2 Measurements

A flame ionization detector is sensitive to compounds which contain C-C or C-H bonds, less sensitive to certain functional groups of organic compounds, such as alcohols, amines, carbonyls, and halogens, and is insensitive towards noncombustible gases, e.g., H_2O, CO_2, SO_2 and NO [*Yuwono and Indrayanto*, 2005]. Therefore, a methanizer must be used in order to be able to detect CO and CO_2 with the FID. A schematic diagram of the custom built methanizer is shown in Figure 13.

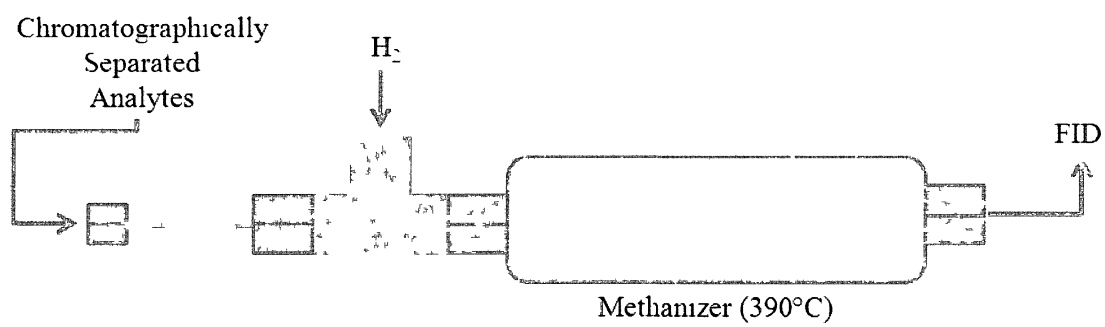

Figure 13. Schematic diagram of the methanizer used for ambient CO and CO_2 measurements.

The methanizer catalytically hydrogenates CO and CO_2 to CH_4 by passing the chromatographically separated analytes through heated tubing with hydrogen (H_2) gas and a nickel (Ni) catalyst (Nickel on silica-alumina, 66.5% as Ni catalyst) (Chemsavers, Inc., Powhatan, Virginia). Furthermore, the reactions of the carbon oxides to yield CH_4 are as follows [*Habazaki et al.*, 1998]:

$$CO + 3H_2 \xrightarrow{Ni} CH_4 + H_2O \quad (2)$$

$$CO_2 + 4H_2 \xrightarrow{Ni} CH_4 + 2H_2O \quad (3)$$

As stated previously, the analytes must be chromatographically separated before they are introduced into the methanizer. This has been explored through tailoring the chromatography via capillary columns and by using separation columns packed with solid adsorbents.

2.1.4. Methodology: Capillary Columns

Instruments that have been developed to measure a similar suite of gases in the literature [e.g., *Van Der Laan et al.*, 2009; *Thompson et al.*, 2009; *Popa et al.*, 2010] use packed columns to achieve separation of the gases from the bulk atmosphere. Capillary columns have obvious advantages over packed columns. These advantages include improved separations with higher resolution, quicker analysis, smaller sample size requirements, and often higher sensitivity [*Grob and Barry*, 1995]. Several capillary columns were experimented with in an attempt to utilize the advantages that they entail.

2.1.4.1. CP-Molsieve 5A Capillary Column

A 30 m x 0.32 mm I.D., 10-μm film thickness CP-Molsieve 5A porous-layer open tubular (PLOT) (Varian, Middelburg, The Netherlands) fused silica column was used in an attempt to separate methane, carbon dioxide and carbon monoxide. This column consists of an alkaline aluminosilicate (pore size of 5 Å with Ca^{2+} as primary cation) stationary phase [*Grob and Barry*, 1995]. A gas standard (Alltech Associates, Inc., Deerfild, IN) ($CO_xC_1C_2$) consisting of 1% components of carbon oxides and C_1-C_2 hydrocarbons (e.g., carbon monoxide, carbon dioxide, methane, acetylene, ethane and ethylene) in a balance of nitrogen was analyzed with a flame ionization detector. The

resulting chromatogram is shown in Figure 14. It is apparent that all analytes detected by the FID are weakly retained by the stationary phase as a co-elution of all the compounds exists at the beginning of the run, effectively saturating the detector.

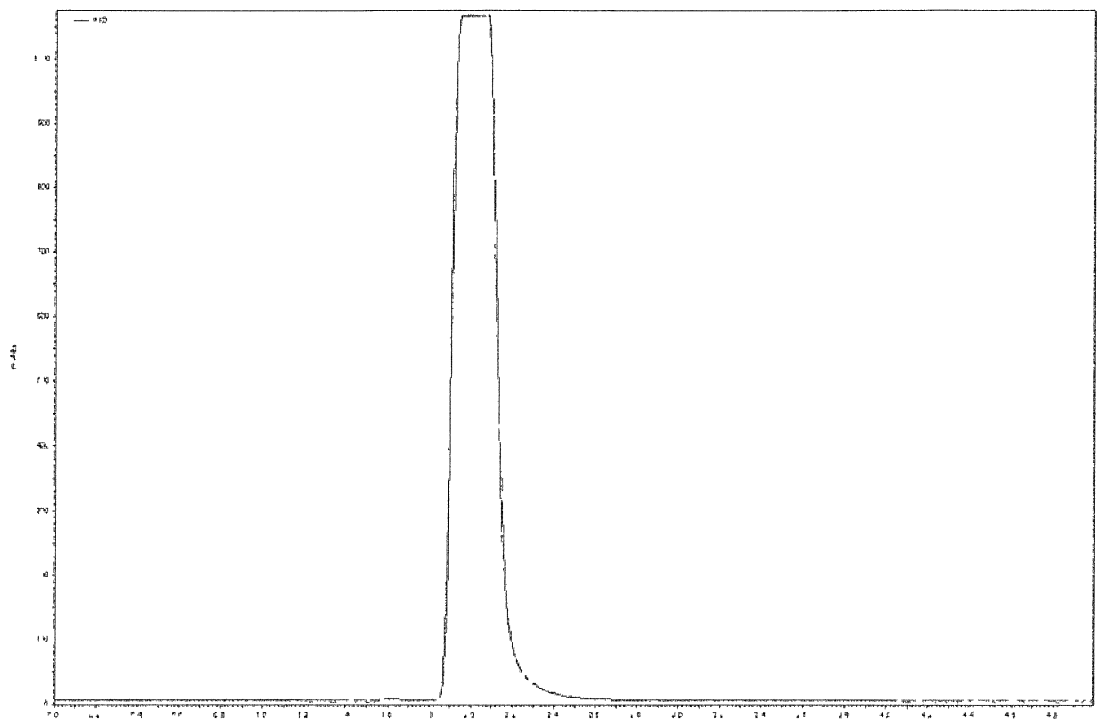

Figure 14. CP-Molsieve 5A PLOT chromatogram of the $CO_xC_1C_2$ gas mixture by FID.

In an effort to achieve a better separation for these low molecular weight gases a Porous-Sil C (10' x 1/8" OD, 80/100 mesh) was added in series with the CP-Molsieve 5A PLOT column. The addition of the Porous-Sil C column appears to have separated the C_1-C_2 hydrocarbons in the gas mixture as four peaks are now present in the chromatogram (Figure 15).

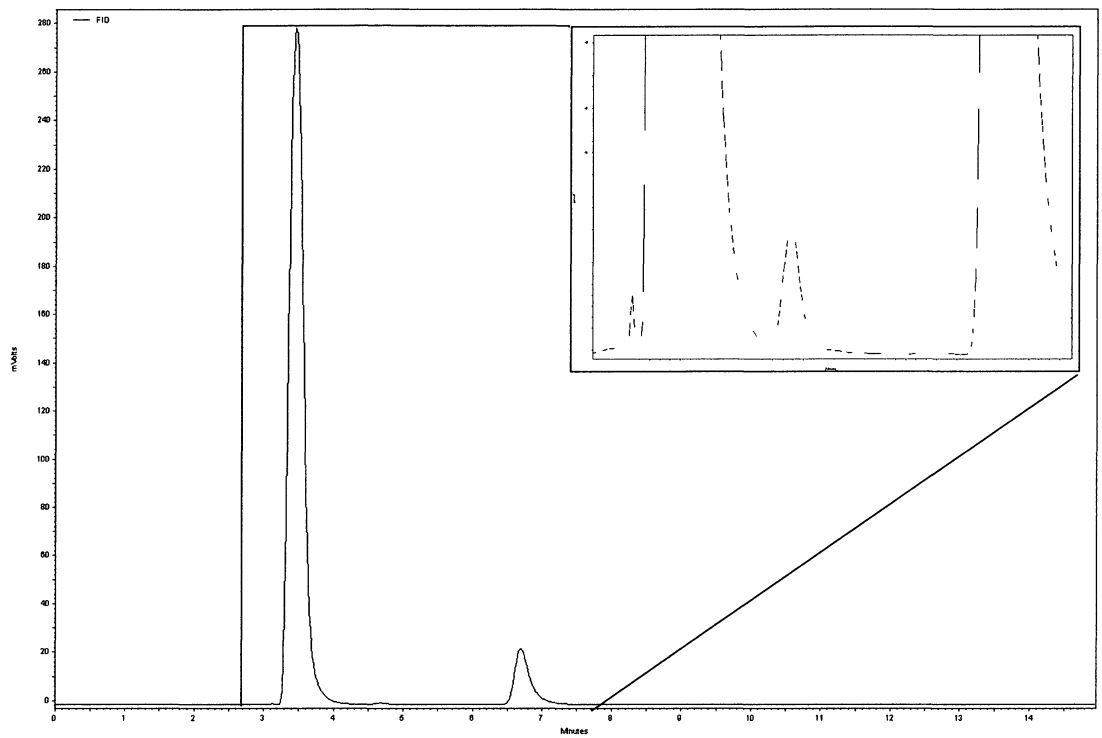

Figure 15. Porous-Sil C/CP-Molsieve 5A PLOT chromatogram of the $CO_xC_1C_2$ gas mixture by FID.

The FID is insensitive to carbon monoxide and carbon dioxide. Therefore, a pulsed discharge helium ionization detector (PDHID) was employed to assess the separation of CH_4, CO and CO_2. The results from analyzing the $CO_xC_1C_2$ gas mixture via PDHID are displayed in Figure 16. This chromatogram highlights the fact that this detector is highly versatile as it is evident that more compounds are detected as there are three peaks, two of which are most likely co-elutions of several compounds resulting in saturation of the detector. Subsequent analysis of this gas mixture revealed that other compounds may be bleeding off of the Porous-Sil C pre-column as the two later eluting peaks have tailing characteristics during subsequent runs (Figure 17).

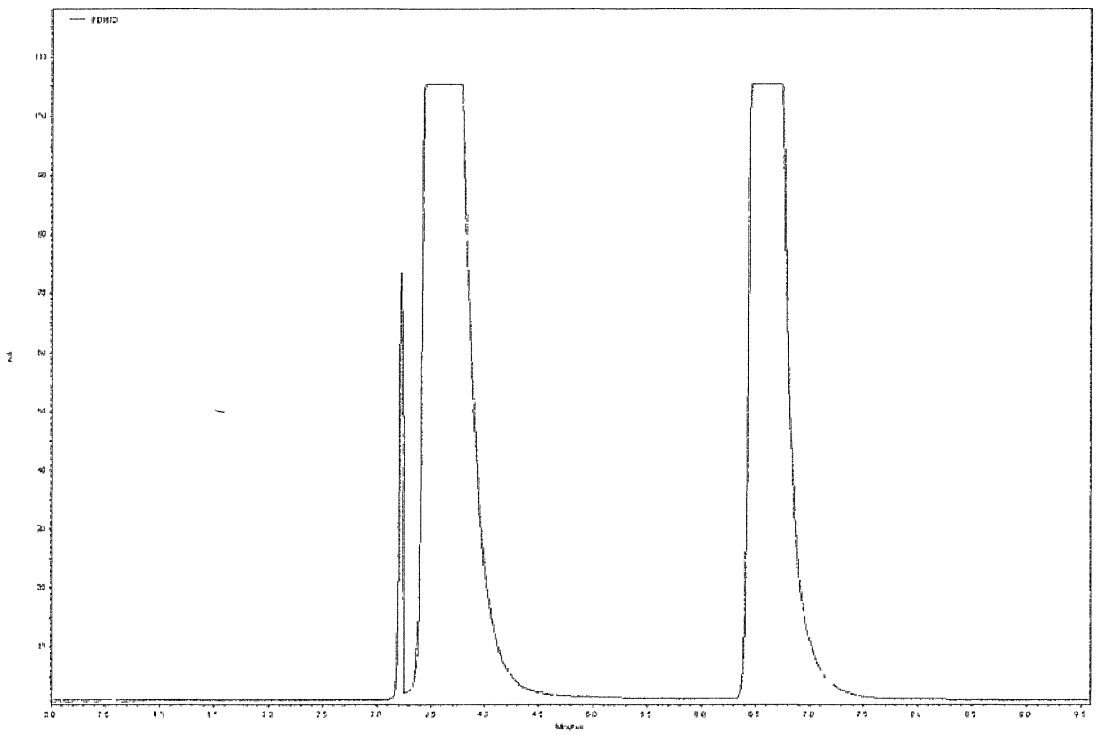

Figure 16. Porous-Sil C/CP-Molsieve 5A PLOT chromatogram of the $CO_xC_1C_2$ gas mixture by PDHID.

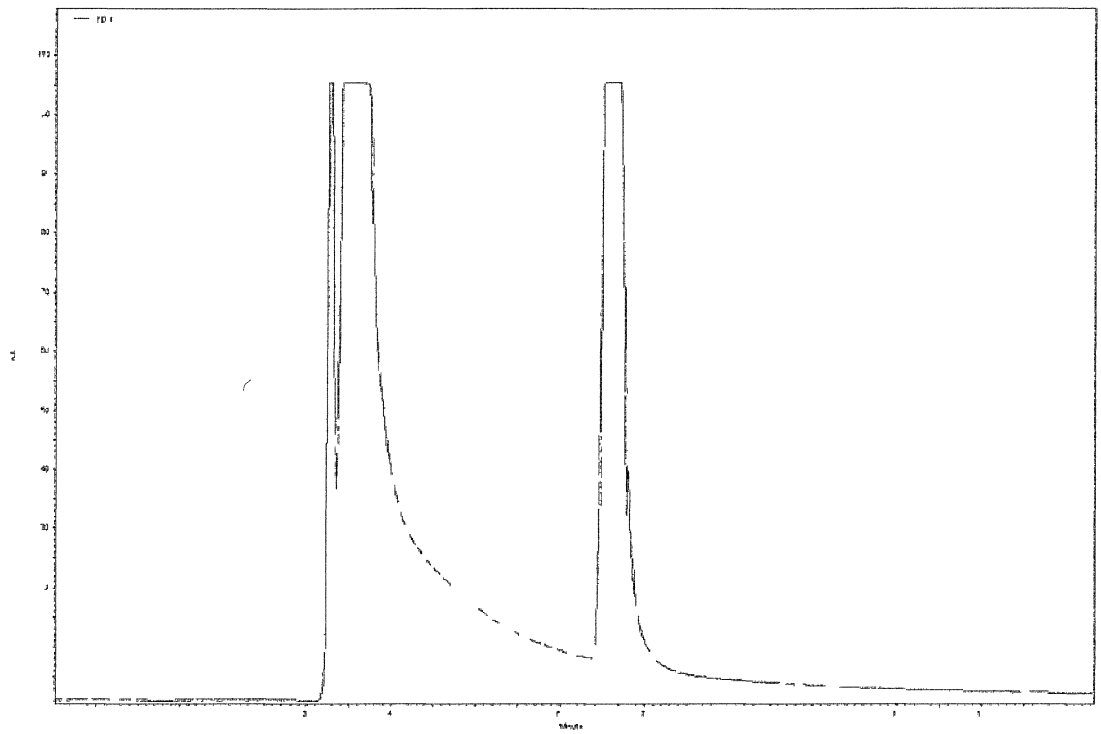

Figure 17. Chromatogram of the subsequent analysis of the $CO_xC_1C_2$ gas mixture by PDHID.

Taking into consideration the fact that the $CO_xC_1C_2$ gas mixture was saturating the detector the mixture was diluted with ultra high purity (UHP) zero air in a 2-L stainless steel sampling canister. The chromatogram that was obtained from this analysis is shown in Figure 18. Analyzing this gas mixture at diluted levels yielded more ideal results as the detector was no longer undergoing saturation and the co-eluting peaks have been partially resolved. However, due to the weak separation of the gases present in the gas mixture with the Porous-Sil C/CP-Molsieve 5A PLOT column combination and the highly universal characteristics of the detector, it was determined that this column detector combination was not going to be ideal for the desired application of the system. Therefore, a packed column chromatographic method was pursued to achieve separations of the analytes of interest from the bulk atmosphere.

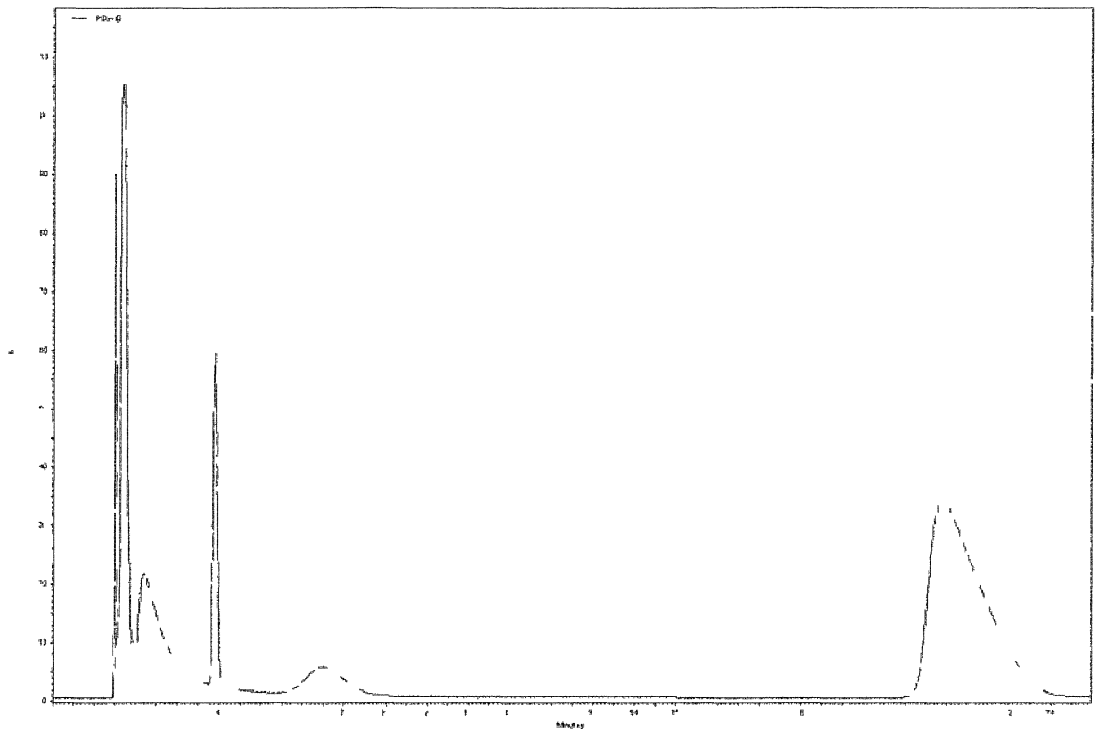

Figure 18. Chromatogram of the diluted $CO_xC_1C_2$ gas mixture by PDHID.

2.1.5. Methodology: Packed Columns

A Shimadzu 17A gas chromatograph (GC) was equipped with a Flame Ionization Detector (FID) and a custom built methanizer for the measurements of CO_2, CH_4 and CO; additionally, the GC was also equipped with an Electron Capture Detector (ECD) used for measurements of N_2O and SF_6. The general parameters of this system are similar to those described in the literature [e.g., *Van Der Laan et al.*, 2009; *Thompson et al.*, 2009; *Popa et al.*, 2010] but with several significant modifications which have improved the overall performance, ultimately proving to make this a superior analytical system.

2.1.5.1. Gas-Solid Chromatography: Porous Polymers and Molecular Sieve Column Packing Materials

The suite of target gases to be quantified were first separated via gas-solid chromatography (GSC), where the analytes undergo surface adsorption on an uncoated column packing or stationary phase [*Grob and Barry*, 1995]. Table 7 lists the compositions of the molecular sieve and porous polymer adsorbents that were both explored and ultimately used to achieve separations of CO_2, CH_4, N_2O, SF_6 and CO from the bulk constituents of the atmosphere. The particle sizes of these adsorbents are described in terms of mesh size, for example 60/80 mesh (the mesh size used primarily in this work) is equivalent to particles which have diameters ranging from 180-250 microns (μm); a conversion chart for mesh sizes is provided in Table 8.

Table 7. Composition of the molecular sieve and porous polymer adsorbent packing materials used for the chromatographic separation columns [*Grob and Barry*, 1995].

Adsorbent	Composition
HayeSep D	high purity divinylbenzene (DVB) polymer
HayeSep Q	divinylbenzene (DVB) polymer
Molecular Sieve 5A	synthetic alkali earth metal aluminum silicate (pore size of 5 Å with Ca^{2+} as primary cation)
Molecular Sieve 13X	synthetic alkaline earth metal aluminum silicate (pore size of 13 Å with Na^{1+} as primary cation)
Porapak Q	ethylvinylbenzene-divinylbenzene (EVB-DVB) copolymer
Porous-Sil C	spherical porous silica

Table 8. Mesh size conversion to particle diameter for column packing materials.

Mesh Size	Microns (μm)
40/60	250-420
60/80	177-250
80/100	149-177
100/120	125-149

2.2. ECD Measurements of N_2O and SF_6

For measurements of N_2O and SF_6, a 2 mL sample loop was flushed continuously with either ambient air, a whole air standard (WA_STD) or a GHG calibration gas mixture (GHG_STD) (Scott-Marrin Inc., Riverside, CA) selected from an upstream stream select valve (SSV) (Valco Instruments Co. Inc., Houston, Texas). The sample was then injected onto the pre-column (Ohio Valley Specialty Company, HayeSep Q, 4' x 1/8" OD, 80/100 mesh) by switching a 10-port two position switching valve, SV_N_2O/SF_6 (Valco Instruments Co. Inc., Houston, Texas) from Position A (load) to Position B (inject) (Figure 19).

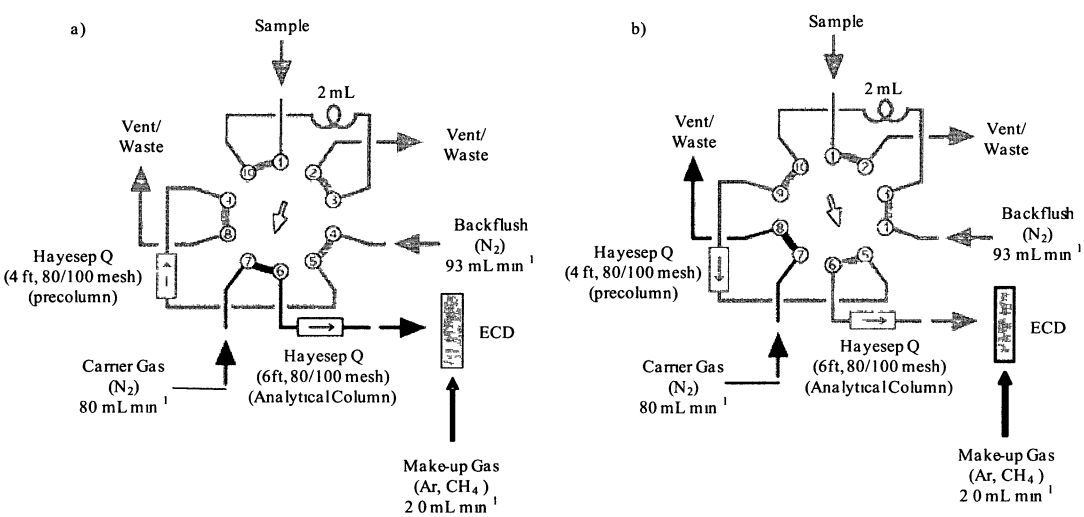

Figure 19. Flow Scheme for the SV_N_2O/SF_6 switching valve in a) load and b) inject.

Once N_2O and SF_6 have eluted from the pre-column they are then transferred to the analytical column (Ohio Valley Specialty Company, HayeSep Q, 6' x 1/8" OD, 80/100 mesh) from which they subsequently eluted to the ECD for detection. Meanwhile, the SV_N_2O/SF_6 was switched back to Position A to effectively backflush later eluting compounds present on the pre-column to waste and to begin flushing the loop preparing for the next sample injection.

A chromatogram obtained without backflushing the later eluting compounds off the pre-column is shown in Figure 20.

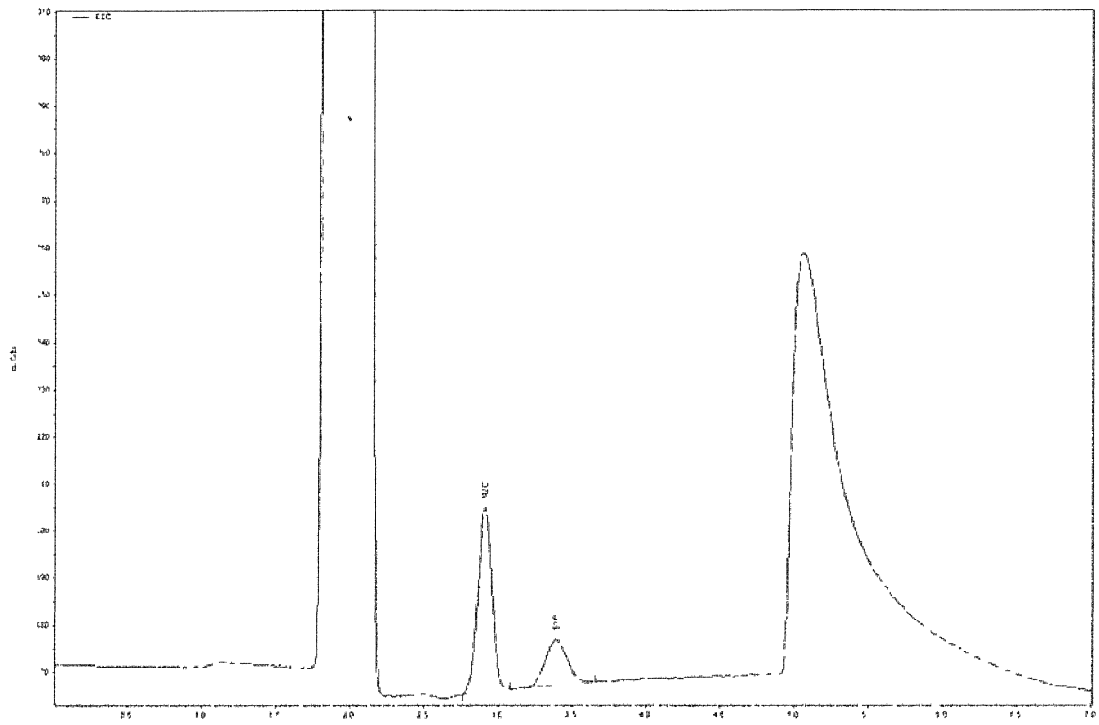

Figure 20. Chromatogram obtained without backflushing later eluting compounds to waste.

When compounds which were more strongly retained than N_2O and SF_6 weren't successfully backflushed off the pre-column, they entered the analytical column and bled off the column during subsequent runs. Therefore, the timing for switching the SV_N_2O/SF_6 back to Position A was essential to successfully allow N_2O and SF_6 to reach the analytical column, without allowing later eluting compounds to exit the pre-column. Figure 21 provides a chromatogram obtained after successfully backflushing later eluting compounds to waste. After achieving the separation of N_2O and SF_6 from the bulk atmospheric constituents, the channel was optimized to improve peak shape and resolution in order to improve the accuracy and precision of the measurements. The peaks

shown in the chromatogram (Figure 21) are not ideal as the N_2O peak is broad and there is limited baseline separation between the two peaks. As a result of an isothermal analysis of N_2O and SF_6 at 45°C, the analytes were not retained optimally on the stationary phase, causing the poor peak shape.

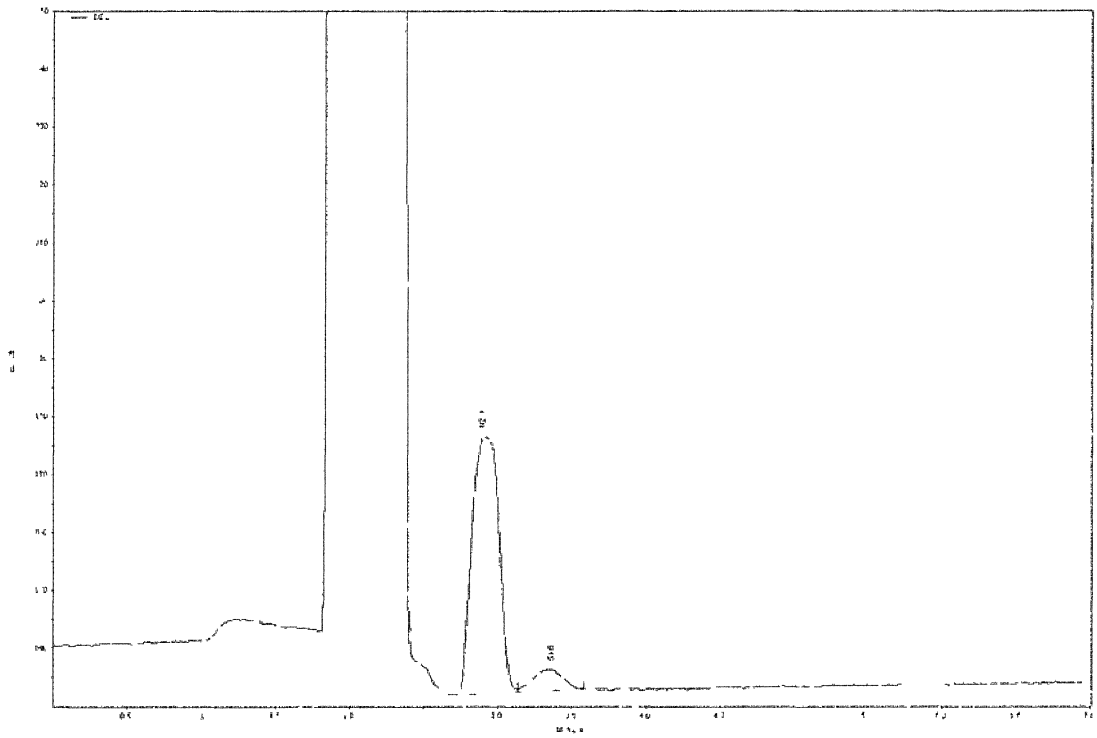

Figure 21. Chromatogram obtained after successfully backflushing later eluting compounds to waste.

To improve the baseline separation for these two peaks, the GC oven temperature was first reduced to 35°C. Decreasing the temperature of the columns decreased zone broadening. In addition, the carrier gas flow rate was increased to 60 mL min^{-1}, which effectively helped to sharpen the N_2O and SF_6 peaks. Finally, the ECD was doped with a small make-up flow (2 mL min^{-1}) of P-5 (95% Argon, 5% Methane) to increase the detector's sensitivity to N_2O. The results obtained after optimizing conditions for the N_2O and SF_6 channel are displayed in Figure 22, where the chromatogram shown with the red

trace represents the initial conditions, the black trace represents optimized conditions and the inserted chromatogram further shows the difference in the abundance and the increased resolution for N_2O and SF_6. Furthermore, the ECD chromatographic trace shown in Figure 22, from left to right, shows the oxygen peak, which is not used for analytical purposes, N_2O and SF_6.

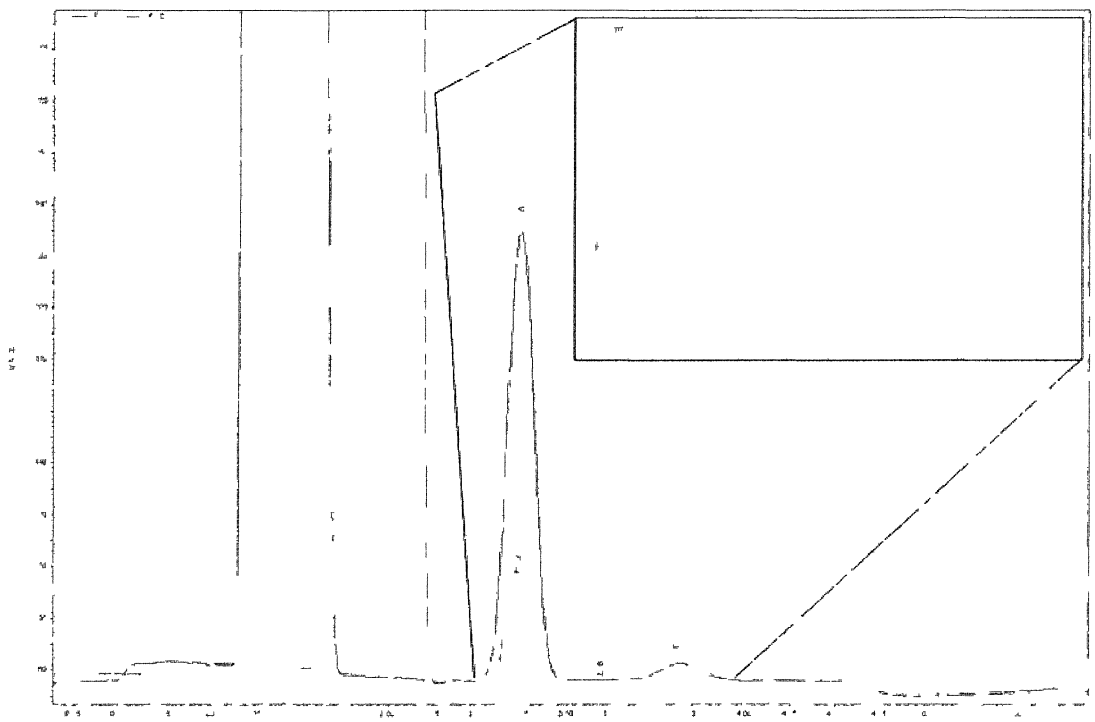

Figure 22. Chromatograms showing initial (red trace) and optimized (black trace) conditions for the ECD channel.

Saturation of the ECD occurred with each analysis as a result of the detector's response to oxygen. Introduction of a significant amount of oxygen to the detector is capable of degrading the ECD, e.g., oxidation of the ^{63}Ni source, and limiting instrument sensitivity. Therefore, a 4-port two position switching valve, SV_ECD (Valco Instruments Co. Inc., Houston, Texas), was employed to effectively remove oxygen (O_2) in the sample, thus, preventing it from entering and degrading the detector. Removal of

O_2 was accomplished by directing the sample effluent to waste by switching the SV_ECD to Position B (load). Once O_2 had been vented to waste, the SV_ECD was switched back to Position A to direct the sample to the detector (inject) (Figure 23). Figure 24 shows a chromatogram of optimized conditions for the ECD channel, from left to right, Figure 24 shows three sequential pressure peaks, caused by switching the SV_ECD valve, N_2O and SF_6.

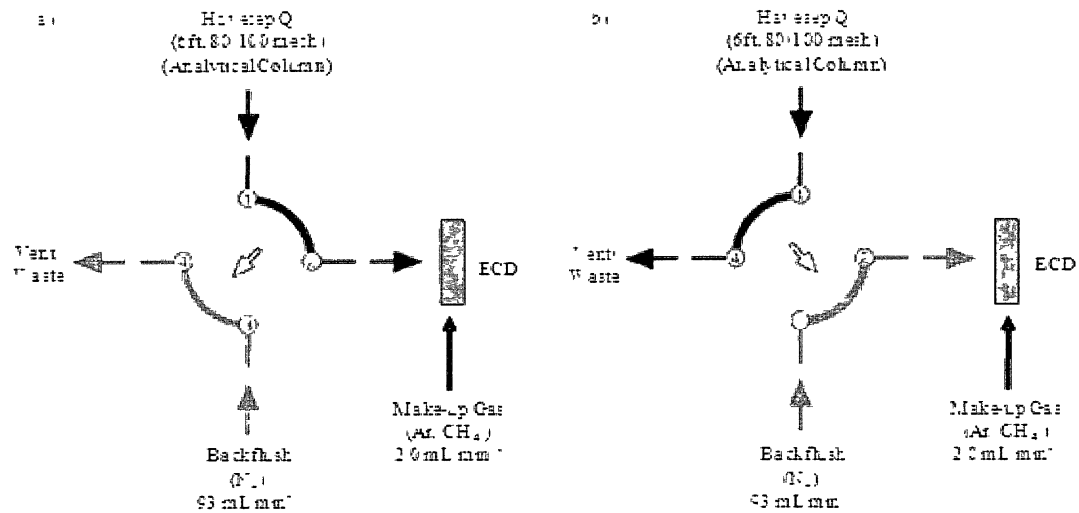

Figure 23. Flow Scheme for the SV_ECD switching valve in a) load and b) inject.

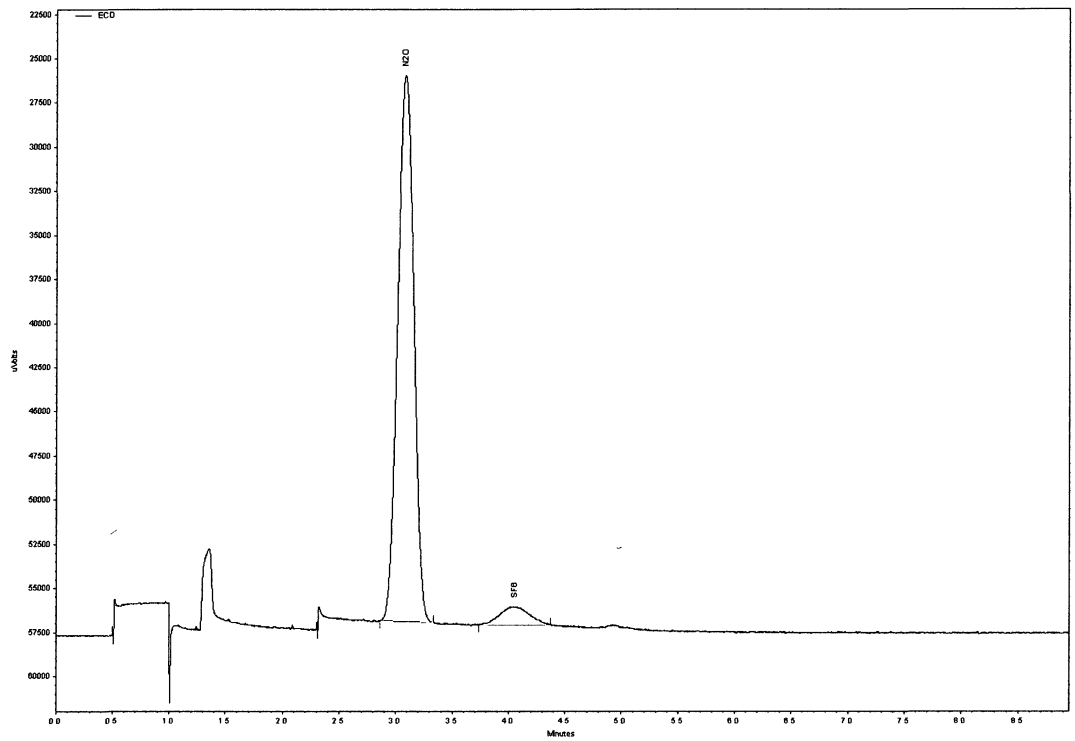

Figure 24. Typical ECD chromatogram of ambient air.

2.3. FID Measurements of CH_4 and CO_2

For ambient measurements of CH_4 and CO_2, a 0.1 mL sample loop was flushed continuously with sample selected from an upstream stream select valve (SSV) (Valco Instruments Co. Inc., Houston, Texas). The sample was then injected onto the analytical column (Ohio Valley Specialty Company, HayeSep Q, 10' x 1/8" OD, 80/100 mesh) by switching a 6-port two position switching valve, SV_CH_4/CO_2 (Valco Instruments Co. Inc., Houston, Texas) from Position A (load) to Position B (inject) (Figure 25).

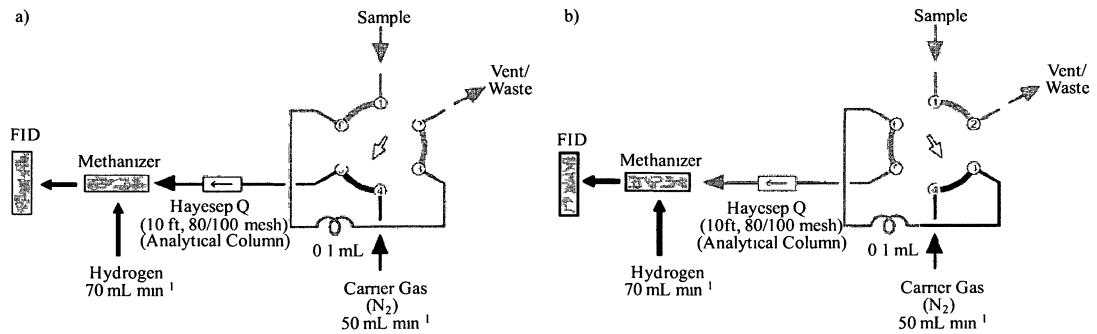

Figure 25. Flow Scheme for the SV_CH_4/CO_2 switching valve in a) load and b) inject positions.

The sample effluent was then directed to waste using a 4-port two position switching valve, SV_Methanizer (Valco Instruments Co. Inc., Houston, Texas), to effectively remove oxygen (O_2) in the sample, thus, preventing it from entering and degrading the methanizer (Figure 30) (refer to 2.4. CO Measurements by FID for a more thorough analysis of the presence/absence of O_2). Once O_2 had been vented to waste, the SV_Methanizer was switched back to Position A to direct the sample through the methanizer and to the FID (Figure 26).

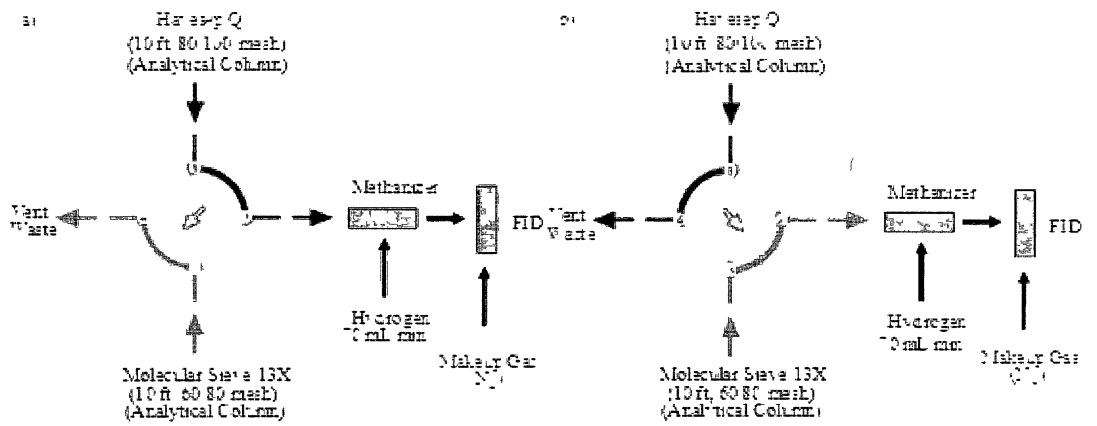

Figure 26. Flow Scheme for the SV_ Methanizer switching valve in a) load and b) inject positions.

A comparison of the chromatographic traces shown in Figures 27 and 28 clearly illustrates the selectivity of the FID and the necessity of the methanizer for CO_2

measurements Figure 27 shows a typical chromatogram of ambient air obtained from analyzing the sample directly with the detector e g , without the catalytic hydrogenation of CO_2 to CH_4, thus, CO_2 is not detected by the FID The chromatographic trace shown in Figure 27, from left to right, shows a small pressure peak, caused by switching the SV_CH_4/CO_2 valve, and then the air peak and CH_4 Figure 28 also shows a chromatographic trace of ambient air, however, in this trace the sample effluent was passed through the methanizer prior to detection The FID chromatogram shown in Figure 28, from left to right, again shows the pressure peak resulting from valve switching (SV_Methanizer) and then CH_4 and CO_2 The insert in Figure 28 further shows the difference in the ambient abundance of CH_4 and CO_2

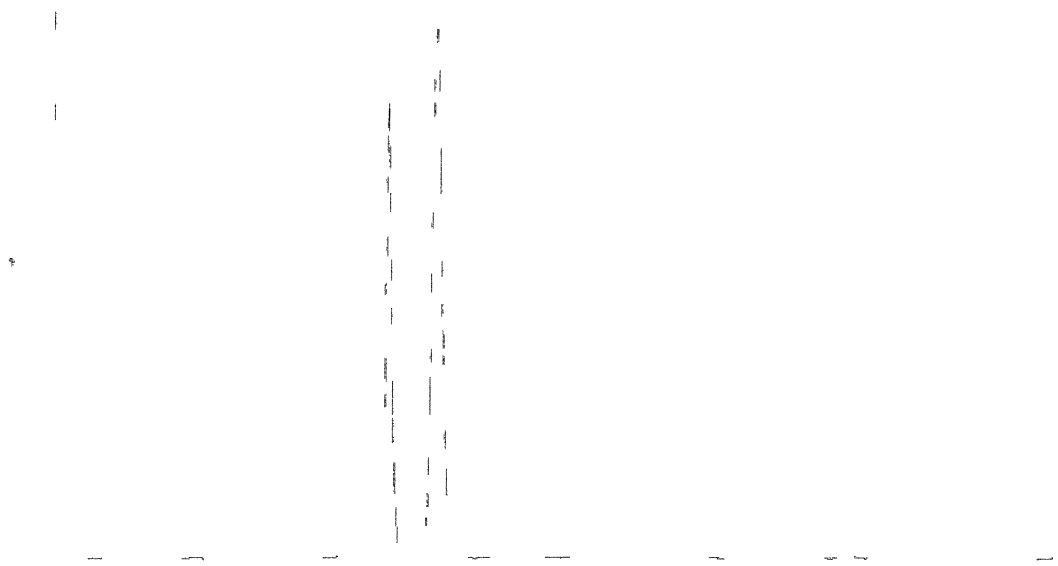

Figure 27. Chromatogram of ambient air analyzed directly with the FID

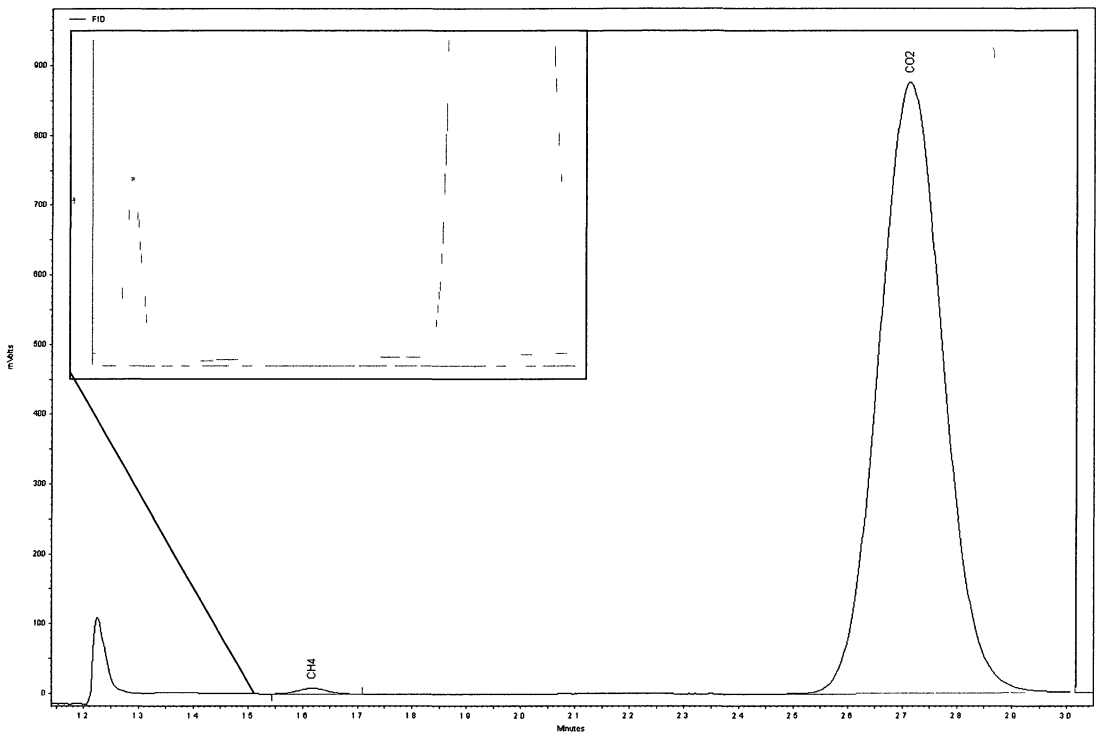

Figure 28. Chromatogram of ambient air after passing the sample through the methanizer.

2.4. CO Measurements by FID

For ambient measurements of CO, a 10 mL sample loop was flushed continuously with sample selected from an upstream stream select valve (SSV) (Valco Instruments Co. Inc., Houston, Texas). The sample was then injected on to two different pre-columns which were connected in series (HayeSep D, 10' x 1/8" OD, 60/80 mesh and Ohio Valley Specialty Company and Porous-Sil C, 10' x 1/8" OD, 80/100 mesh) by switching a 10-port two position switching valve, SV_CO (Valco Instruments Co. Inc., Houston, Texas) from Position A (load) to Position B (inject) (Figure 29). Once CO had eluted from the pre-columns, it was transferred to the analytical column (Molsieve 13X, 10' x 1/8" OD, 60/80 mesh). The sample was then directed to waste using a 4-port two position switching valve, SV_Methanizer (Valco Instruments Co. Inc., Houston, Texas) for removal of O_2 (Position B) (Figure 26). Then the SV_Methanizer was switched to

Position A to direct the sample through the methanizer. Meanwhile, the SV_CO was switched back to Position A to effectively backflush later eluting compounds present on the pre-column to waste and to begin flushing the next sample.

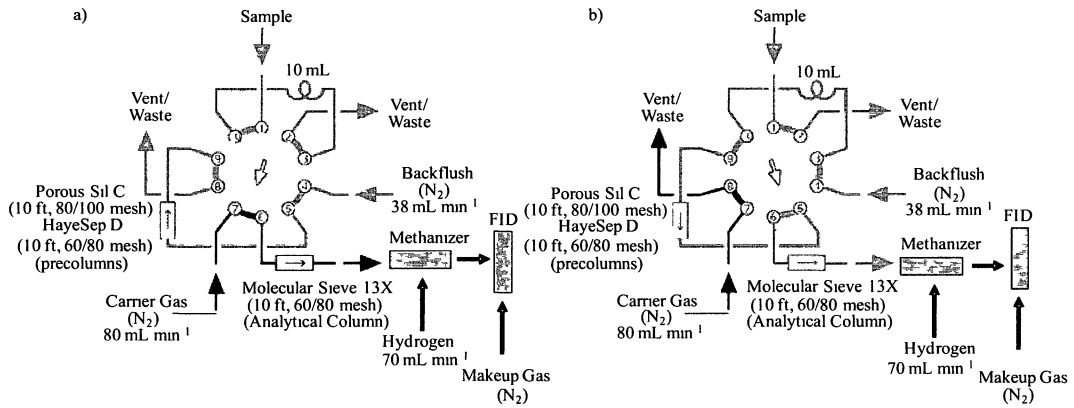

Figure 29. Flow Scheme for the SV_ CO switching valve in a) load and b) inject positions.

The combination of the HayeSep D and Porous-Sil C pre-columns serve to effectively separate CH_4 and CO_2 from CO. This separation is achievable as CO is weakly retained by the two stationary phases while CH_4 and CO_2 are more strongly retained. Several pre-columns and pre-column combinations were explored before deciding on the HayeSep D and Porous-Sil C combination to separate CO from the bulk atmospheric gases. The columns evaluated for CO separation included the following: a Porapak Q pre-column with a Molecular Sieve 5A analytical column (as described by *Van der Laan et al.*, [2009]), a Porapak Q pre-column with a HayeSep Q analytical column, a HayeSep D pre-column with a Porapak Q analytical column, a Porous-Sil C pre-column with a Molecular Sieve 5A analytical column and finally a combination of HayeSep D and Porous-Sil C pre-columns with a Molecular Sieve 5A analytical column. The pre-columns and analytical columns explored could not provide adequate separation

of CO from CH_4 in ambient air. For instance, the elution order of gases observed with the Porapak Q pre-column was CO, CH_4 then CO_2, with a weak separation present for CO and CH_4. The elution order observed with the Molecular Sieve 5A analytical column was CH_4, CO then CO_2. Therefore, when the analytes passed through the analytical column a co-elution of CH_4 and CO was observed. Similarly, as with the other column combinations, the inability to separate CO and CH_4 was a recurring issue until the combination of HayeSep D and Porous-Sil C pre-columns were employed. Using these two columns in series, it was possible to retain CH_4 and CO_2 more strongly, such that they would nearly co-elute, while CO passed through the columns with little retention. The increased retention times for CH_4 and CO_2 which allowed sufficient time for CO to elute on to the analytical column, while preventing CH_4 and CO_2 from exiting the pre-columns.

Although CO was successfully separated and transferred to the Molecular Sieve 5A analytical column, the observed peak for ambient levels of CO was very broad and difficult to accurately quantify because of the low signal to noise ratio. Therefore, the Molecular Sieve 5A column was replaced with a Molecular Sieve 13X analytical column; this resulted in a reduced retention for CO and corresponded to a sharper chromatographic peak.

As stated previously, a 4-port two position switching valve, SV_Methanizer (Valco Instruments Co. Inc., Houston, Texas) was used for the removal of O_2 from the sample before passing it through the methanizer. Figure 30 shows a comparison of chromatographic traces when O_2 passes through the methanizer (red trace) and when O_2 was vented to waste prior to the sample passing through the methanizer (black trace). The

chromatograms in Figure 30 were obtained from analyzing a sample of 484 parts per billion by volume (ppbv) of CO. The red trace shows a negative spike in the baseline at ~ 4.65 min, followed by a very noisy baseline which may be indicative of O_2 peak fractionation or oxidation of the Ni catalyst. At a CO mixing ratio of 484 ppbv this "noise" doesn't cause a large deviation from the results obtained from analyzing an O_2 free aliquot (black trace), but at trace levels in the atmosphere the negative spike and the subsequent baseline spiking results in an undetectable peak for CO. Finally, the FID chromatogram shown in Figure 30 (black trace), from left to right, exhibits a pressure spike caused by switching SV_Methanizer and then the cleanly resolved CO peak.

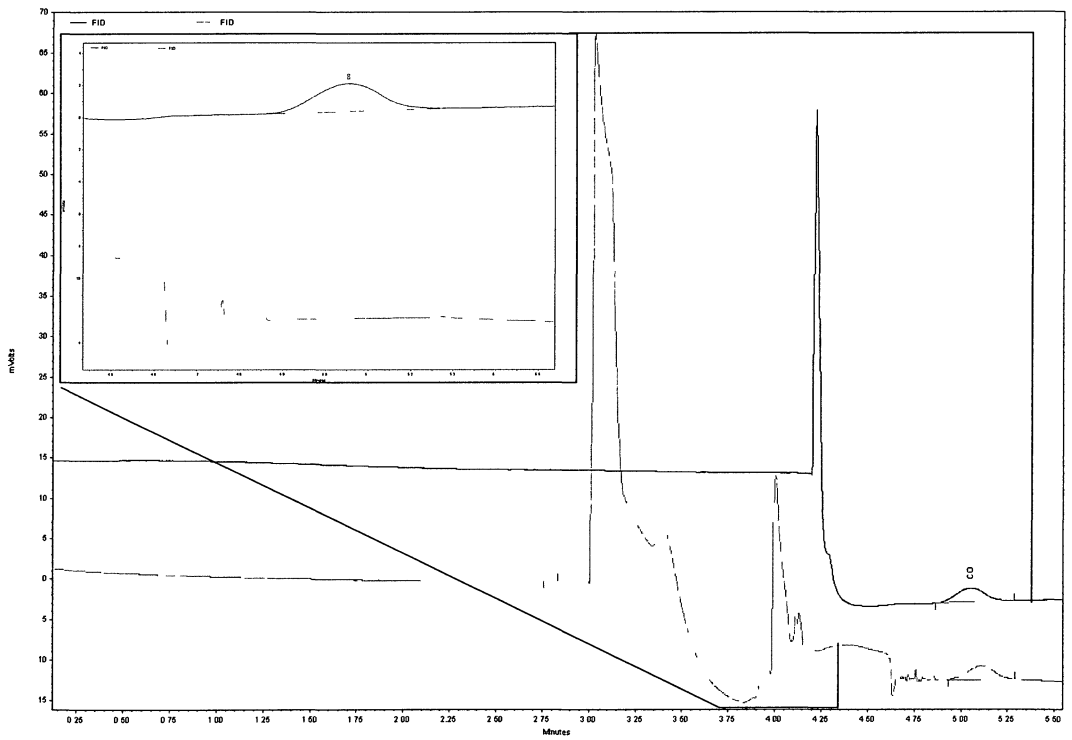

Figure 30. Chromatograms of 484 ppbv of CO with O_2 (red trace) and without O_2 in the sample.

2.5. Summary

A three-channel, two-detector system was constructed to measure a suite of greenhouse gases. Figures 31 and 32 show detailed schematic diagrams of the Greenhouse Gas GC analytical system displaying the different configurations that the system undergoes during an analysis. A total of two 10-port SVs are used for the N_2O/SF_6 and CO channels while the CO_2/CH_4 channel uses a 6-port SV, which is in series with the CO channel. Sample streams from the CO and CH_4/CO_2 channels are directed through the methanizer with a 4-port SV and the sample stream from the N_2O/SF_6 channel is directed to the ECD with a 4-port SV. Two needle valves, located downstream of the SSV, are used to direct the sample through the three sample loops. The N_2O/SF_6 channel sample loop was maintained at 44.7 psi while the N_2O/SF_6 and CO channels were maintained at 18.7 psi. Finally, in an effort to minimize the consumption of gases needed, particularly due to the fact that the instrument is to be deployed in the field, only two detectors are used.

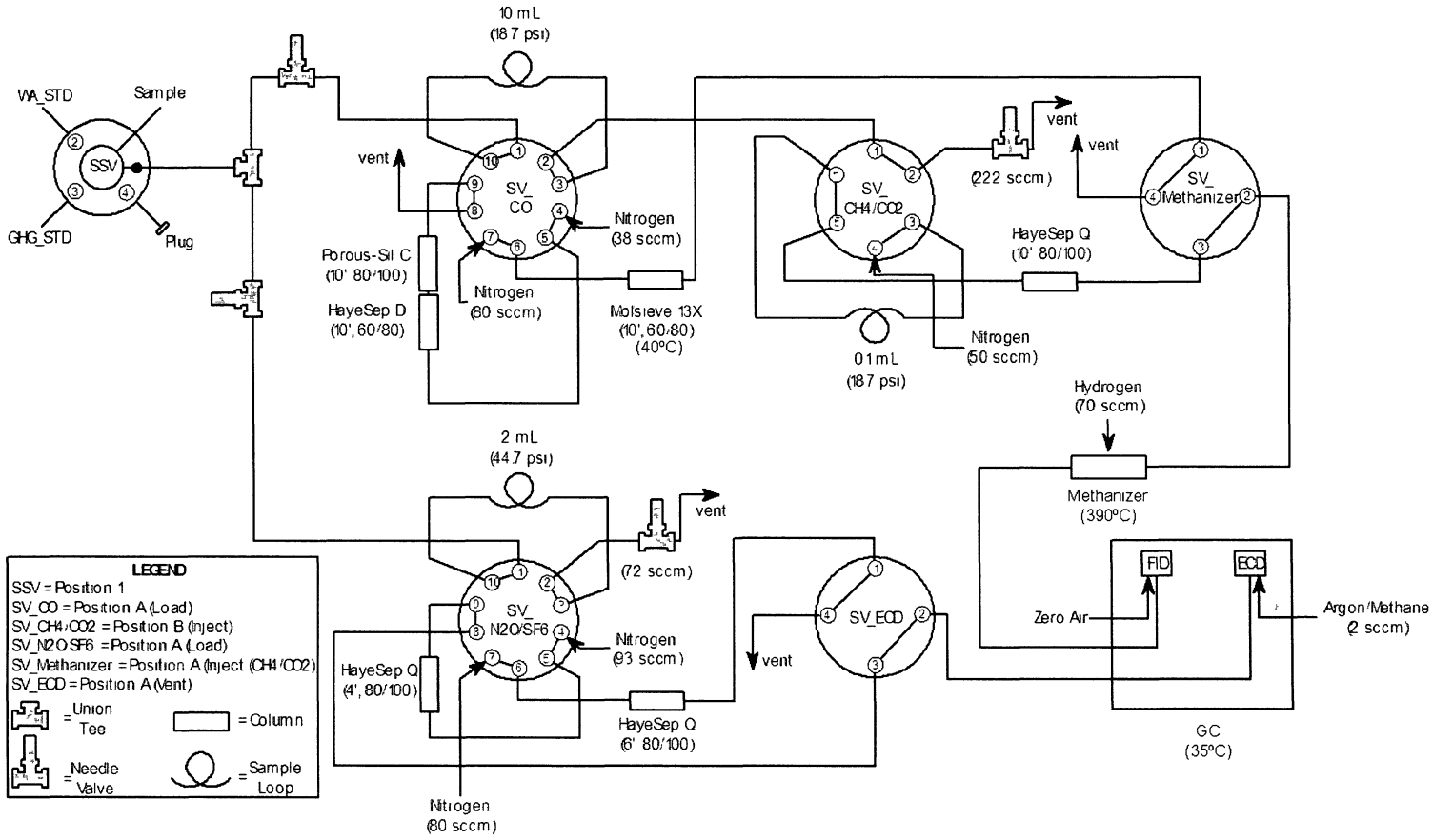

Figure 31. Schematic diagram of the Greenhouse Gas GC analytical system (a).

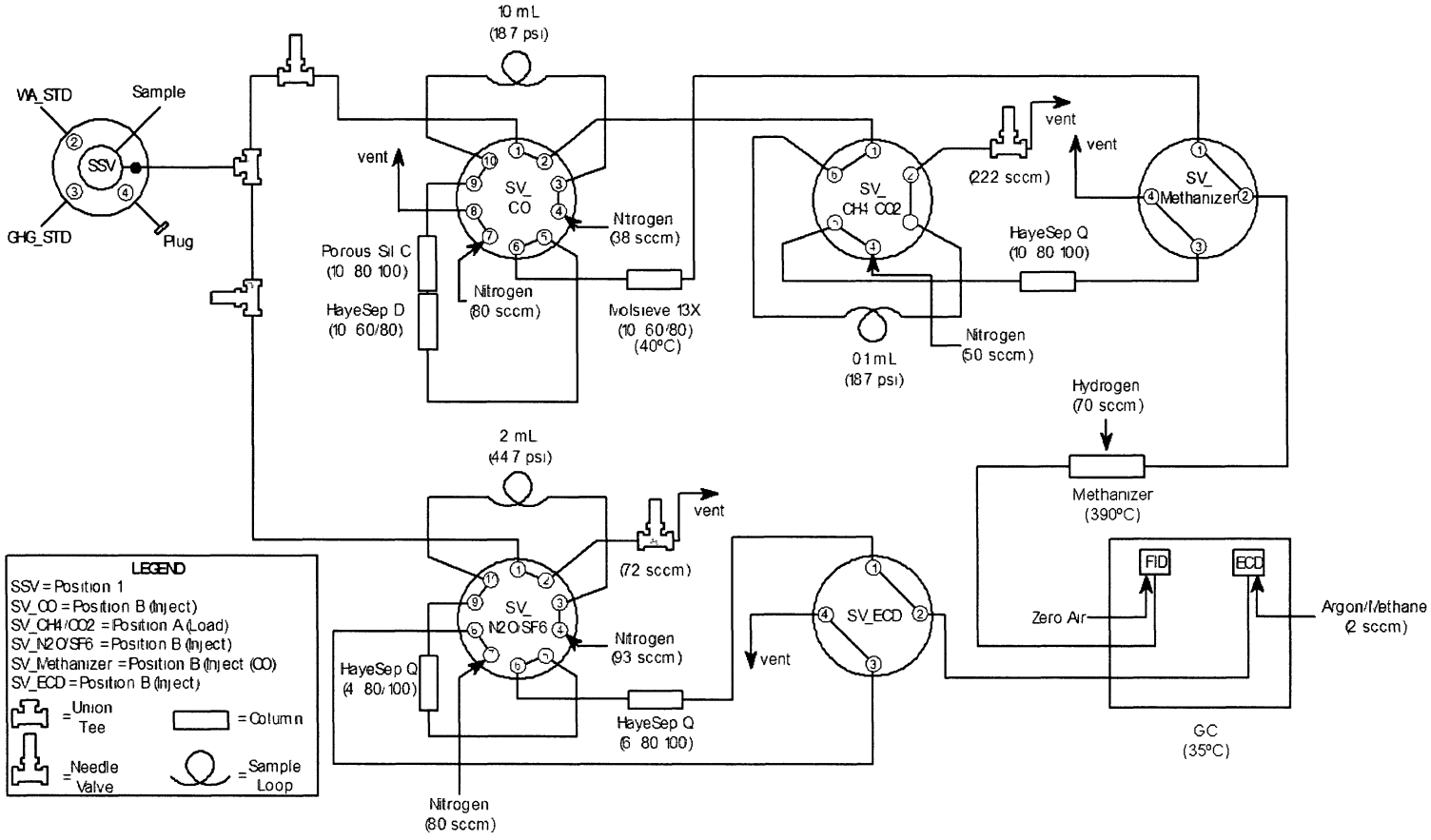

Figure 32. Schematic diagram of the Greenhouse Gas GC analytical system (b).

CHAPTER 3

RESULTS AND DISCUSSION

3.1. Quantification of Analytes

For quantitative analysis, peak height and peak area were examined for the suite of gases analyzed with the greenhouse gas GC system. Table 9 provides the results from a precision assessment of the calibration standard using both peak height and peak area for quantification. Based on these results, improved precision was obtained using peak height for analyte quantification.

Table 9. Relative standard deviations (RSD) obtained from peak height and peak area for analyte quantification.

Atmospheric Species	Peak Height RSD (%)	Peak Area RSD (%)
CO	1.91	4.37
CH_4	1.09	1.47
CO_2	2.74	2.76
N_2O	0.21	0.27
SF_6	1.46	2.02

The FID and ECD each have a unique response for the target compounds on both channels; therefore, a response factor (or calibration factor) is needed to obtain meaningful quantitative data. The response factor was obtained experimentally by analyzing a known quantity of a standard of known composition and measuring the height of the corresponding peak. Thus, a response factor (RF) for each of the greenhouse

gases was determined by dividing the peak height (H) (or area, A) by the mixing ratio of the calibration standard (MR) [e.g., *Sive*, 1998] as follows:

$$RF = \left(\frac{H}{MR} \right) \tag{2}$$

Furthermore, the response factor for each of the atmospheric gases analyzed (RF_x) determined from the calibration standard (GHGSTD) can be used to determine the mixing ratios of the given species (C_x) in an ambient air sample when the peak height (H_x) (or area, A_x) is measured;

$$C_x = \left(\frac{H_x}{RF_x} \right) \tag{3}$$

Table 10 lists the experimentally determined mixing ratios (from equations 2 and 3) of the working standard, i.e., the whole air standard (WASTD), which is used for system diagnostics as well as secondary calibrations.

Table 10. Experimentally determined mixing ratios of the whole air standard (WASTD).

Compound	Mixing Ratio
Carbon Monoxide	536±7.2 ppbv
Methane	1.9±0.01 ppmv
Carbon Dioxide	376±1.5 ppmv
Nitrous Oxide	442±0.60 ppbv
Sulfur Hexafluoride	7.3±0.16 pptv

3.2. Method Development and Sampling Scheme

Complete instrument automation has been achieved for the GHG system, encompassing the quantitative analysis for all five target gases in a single analytical run. The system is currently configured to measure continuous, *in situ* atmospheric mixing ratios of CO_2, CH_4, N_2O, SF_6 and CO. The SSV, two 10-port SVs, two 4-port SVs and the 6-port SV actuators are all controlled with a PC and two Agilent SS420x instrument interface boxes (analog-to-digital converters); each of the valve actuators are wired to the

relay outputs in the interface box. Configuration of the interface box for valve/event control coupled with the chromatographic data processing software, EZStart™, allowed for automated operation of the actuator(s). Table 11 shows the external events methods developed for samples of a) ambient air, b) the calibration standard (GHGSTD) and c) the working standard (WASTD), with the GHGSTD and WASTD mixing ratios listed in Table 12 .

Table 11. External event methods developed for the analysis of a) ambient air, b) WASTD and c) GHGSTD.

a)

Ambient Air			
Event	**Time (min)**	**Duration (min)**	**Valve State**
N_2O/SF_6_Load	0.50	0.50	Closed
CO_Load	0.50	0.50	Closed
N_2O/SF_6_Inject	1.00	6.00	Closed
CO_Inject	1.00	2.50	Closed
CO_Load	3.50	3.00	Closed
CO_Meth_FID	4.35	2.15	Closed
CO_2/CH_4_Meth_FID	4.35	-	Open
CO_2/CH_4_Load	5.30	0.50	Closed
CO_2/CH_4_Inject	5.80	4.50	Closed
CO_2/CH_4_Meth_FID	6.50	5.00	Closed
CO_Meth_FID	6.50	-	Open
N_2O/SF_6_Load	7.00	-	Closed

Table 11 (continued). External event methods developed for the analysis of a) ambient air, b) WASTD and c) GHGSTD.

b)

WASTD			
Event	**Time (min)**	**Duration (min)**	**Valve State**
N_2O/SF_6_Load	0.50	0.50	Closed
CO_Load	0.50	0.50	Closed
SSV_Home	0.50	-	Open
SSV_Step	0.50	0.50	Closed
N_2O/SF_6_Inject	1.00	6.00	Closed
CO_Inject	1.00	2.50	Closed
SSV_Home	1.00	4.30	Closed
SSV_Step	1.00	-	Open
CO_Load	3.50	3.00	Closed
CO_Meth_FID	4.35	2.15	Closed
CO_2/CH_4_Meth_FID	4.35	-	Open
CO_2/CH_4_Load	5.30	0.50	Closed
SSV_Home	5.30	0.50	Open
SSV_Step	5.30	0.50	Closed
CO_2/CH_4_Inject	5.80	4.50	Closed
SSV_Home	5.80	-	Closed
SSV_Step	5.80	-	Open
CO_2/CH_4_Meth_FID	6.50	5.00	Closed
CO_Meth_FID	6.50	-	Open
N_2O/SF_6_Load	7.00	-	Closed

Table 11 (continued). External event methods developed for the analysis of a) ambient air, b) WASTD and c) GHGSTD.

c)

GHGSTD			
Event	**Time (min)**	**Duration (min)**	**Valve State**
N_2O/SF_6_Load	0.50	0.50	Closed
CO_Load	0.50	0.50	Closed
SSV_Home	0.48	-	Open
SSV_Step	0.48	-	Closed
SSV_Step	0.49	-	Open
SSV_Step	0.50	-	Closed
N_2O/SF_6_Inject	1.00	6.00	Closed
CO_Inject	1.00	2.50	Closed
SSV_Home	1.00	4.30	Closed
SSV_Step	1.00	-	Open
CO_Load	3.50	3.00	Closed
CO_Meth_FID	4.35	2.15	Closed
CO_2/CH_4_Meth_FID	4.35	-	Open
CO_2/CH_4_Load	5.30	0.50	Closed
SSV_Home	5.28	-	Open
SSV_Step	5.28	-	Closed
SSV_Step	5.29	-	Open
SSV_Step	5.30	-	Closed
CO_2/CH_4_Inject	5.80	4.50	Closed
SSV_Home	5.80	-	Closed
SSV_Step	5.80	-	Open
CO_2/CH_4_Meth_FID	6.50	5.00	Closed
CO_Meth_FID	6.50	-	Open
N_2O/SF_6_Load	7.00	-	Closed

Table 12. Mixing ratios in the GHGSTD and WASTD.

Atmospheric Species	GHGSTD Mixing Ratio	WASTD Mixing Ratio
Carbon Monoxide	189±18.9 ppbv	536±7.2 ppbv
Methane	2.03±0.04 ppmv	1.9±0.01 ppmv
Carbon Dioxide	404±8 ppmv	376±1.5 ppmv
Nitrous Oxide	350 ppbv	442±0.60 ppbv
Sulfur Hexafluoride	10.5±1.05 pptv	7.3±0.16 pptv

Once the methods were developed for standards and samples, a sequence was written to enable the system to run unattended for prolonged time periods. The sequence was constructed as follows:

$$(AmbientAir)_3 - GHGSTD - (AmbientAir)_3 - WASTD - (AmbientAir)_3 - GHGSTD$$

The cycle time for each individual analysis was 12 minutes, allowing for 120 analyses per day, i.e., 90 ambient air, 15 calibration standard and 15 whole air standard analyses. Moreover, the frequent analyses of the standards provide an important diagnostic tool in order to monitor detector drift and system malfunctions, thus ensuring high quality results are obtained.

An assessment of the system's performance, using the sequence above, revealed variability in the sample inlet line selection, e.g., occasionally when the GHGSTD method was run the sample would be obtained from the whole air standard cylinder rather than the greenhouse gas standard. Ultimately, the short intervals in between switching of the stream select valve (SSV) did not provide sufficient time for the valve to switch to the assigned positions, e.g., SSV_Home, SSV_Step, SSV_Step, etc (refer to 3.3.2. Instrument Precision). Therefore, the GHGSTD method was adjusted such that time intervals were increased slightly allowing sufficient time for the SSV to switch to the desired positions. Also, the GHGSTD and WASTD methods were modified such that the SSV was switched from SSV_Home to SSV_Step, i.e., position 2, to allow pressure equilibration at 6.6 min instead of at 12 min, as the method was previously set. These method modifications (Table 13) significantly improved the measurement precision (refer to 3.3.2. Instrument Precision) and also made the system more robust.

Table 13. Modified external events methods developed for the analysis of a) WASTD and b) GHGSTD.

a)

WASTD			
Event	**Time (min)**	**Duration (min)**	**Valve State**
SSV_Step	0.10	-	Open
N_2O/SF_6_Load	0.50	0.50	Closed
CO_Load	0.50	0.50	Closed
SSV_Step	0.50	0.50	Closed
N_2O/SF_6_ECD	0.50	-	Open
N_2O/SF_6_Vent	0.50	1.80	Closed
N_2O/SF_6_Inject	1.00	3.80	Closed
CO_Inject	1.00	2.50	Closed
SSV_Home	1.00	-	Closed
SSV_Home	1.01	-	Open
SSV_Step	1.01	4.28	Closed
N_2O/SF_6_ECD	2.30	-	Closed
CO_Load	3.50	3.00	Closed
CO_Meth_FID	4.38	2.82	Closed
CO_2/CH_4_Meth_FID	4.38	-	Open
N_2O/SF_6_Load	4.80	-	Closed
SSV_Step	6.01	-	Open
CO_2/CH_4_Load	6.02	0.50	Closed
SSV_Home	6.52	-	Closed
SSV_Home	6.60	-	Open
SSV_Step	6.60	5.40	Closed
CO_2/CH_4_Meth_FID	7.20	5.00	Closed
CO_Meth_FID	7.20	-	Open

Table 13 (continued). Modified external events methods developed for the analysis of a) WASTD and b) GHGSTD.

b)

GHGSTD			
Event	**Time (min)**	**Duration (min)**	**Valve State**
SSV_Step	0.10	-	Open
SSV_Step	0.40	-	Closed
SSV_Step	0.45	-	Open
CO_Load	0.50	0.50	Closed
N_2O/SF_6_Vent	0.50	1.80	Closed
SSV_Step	0.50	0.50	Closed
N_2O/SF_6_Load	0.50	0.50	Closed
N_2O/SF_6_ECD	0.50	--	Open
N_2O/SF_6_Inject	1.00	3.80	Closed
CO_Inject	1.00	2.50	Closed
SSV_Home	1.00	-	Closed
SSV_Home	1.01	-	Open
SSV_Step	1.01	4.79	Closed
N_2O/SF_6_ECD	2.30	-	Closed
CO_Load	3.50	3.00	Closed
CO_Meth_FID	4.38	2.82	Closed
CO_2/CH_4_Meth_FID	4.38	-	Open
N_2O/SF_6_Load	4.80	-	Closed
SSV_Step	5.80	-	Open
SSV_Step	5.90	-	Closed
SSV_Step	6.00	-	Open
SSV_Step	6.02	0.50	Closed
CO_2/CH_4_Load	6.02	0.50	Closed
SSV_Home	6.52	-	Closed
CO_2/CH_4_Inject	6.52	4.50	Closed
SSV_Step	6.60	5.40	Closed
SSV_Home	6.60	-	Open
CO_Meth_FID	7.20	-	Open
CO_2/CH_4_Meth_FID	7.20	5.00	Closed

3.3. System Performance

3.3.1. Methanizer Efficiency

After operating the instrument continuously in excess of a month (6 January to 15 February 2011), it was evident that the methanizer was, in fact, robust and efficient for the hydrogenation of CO and CO_2 to CH_4. The methanizer efficiency was evaluated by examining the response to the concentration ratio of CO_2 to that of CH_4 for a well-known standard, e.g., GHGSTD, since for a given cylinder the ratio of the mixing ratios of CO_2

to CH_4 should be constant and therefore, the ratio of their responses should be constant [*Van der Laan*, 2009]. Figure 33 shows a time series plot of the methanizer efficiency to the response/concentration ratio of CO_2/CH_4; the ratio is constant over this time period with a relative standard deviation (RSD) of 0.52%. These results provide confidence in the reliability of the methanizer's reduction efficiency.

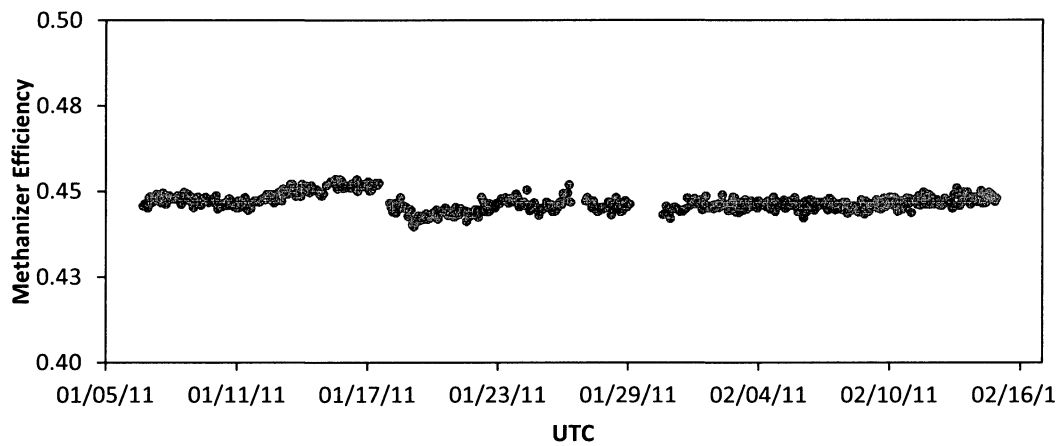

Figure 33. The efficiency of the methanizer using the response to concentration ratio of CO_2 to CH_4 in the GHGSTD at Thompson Farm 2 from January 6 to February 15, 2011.

3.3.2. Instrument Precision

The results from the initial precision assessment (November 6-8, 2010) of the instrument using peak area for analyte quantification are presented in Table 14.

Table 14. Measurement precision improvements of the GHGSTD.

Compound	November 6-8, 2010 RSD (%)	December 21-23, 2010 RSD (%)	December 23-26, 2010 RSD (%)
Carbon Monoxide	17.7	9.81	0.71
Methane	0.73	0.54	0.38
Carbon Dioxide	0.63	2.68	0.29
Nitrous Oxide	1.48	8.72	0.22
Sulfur Hexafluoride	2.94	10.0	0.37

From these results, it is apparent that high measurement precision was achieved for CO_2, CH_4 and N_2O from the GHGSTD, although improvements for SF_6 were desirable and

necessary for CO. The measurement precision of CO_2, CH_4 and N_2O provides confidence in the GHGSTD's integrity and the system's overall performance. Because SF_6 is at a very low mixing ratio in the GHGSTD (10.5 parts per trillion by volume (pptv)), the measurement precision was improved through manual peak integration, where inconsistencies in the auto-integration resulting from baseline noise was likely the major driver of these results. The molecular sieve 13X analytical column for the CO channel was hand-packed in the laboratory and recently conditioned by flowing a UHP dry inert gas (N_2) through the column coupled with baking the column for 12 hours at 120°C. It is likely that the poor precision observed for the CO column was likely a result of incomplete conditioning. Therefore, chromatographic peaks were manually integrated and the analytical column was re-conditioned in an attempt to improve the precision for SF_6 and CO.

The results of the measurement precision using the peak area quantification method achieved subsequent to these modifications are shown in Table 14 (December 21-23, 2010). It is apparent that the measurement precision has improved for methane and carbon monoxide, although the precision for CO was still not ideal. Also, the precision of carbon dioxide, nitrous oxide and sulfur hexafluoride measurements diminished significantly. Further investigation revealed inconsistencies in the sample selection during analyses as described in section 3.2. (Methods Development and Sampling Scheme). Figure 34 shows an example of this phenomenon during the GHGSTD method analysis where there were several occasions (high peak height values) in which the whole air standard was selected rather than the GHGSTD.

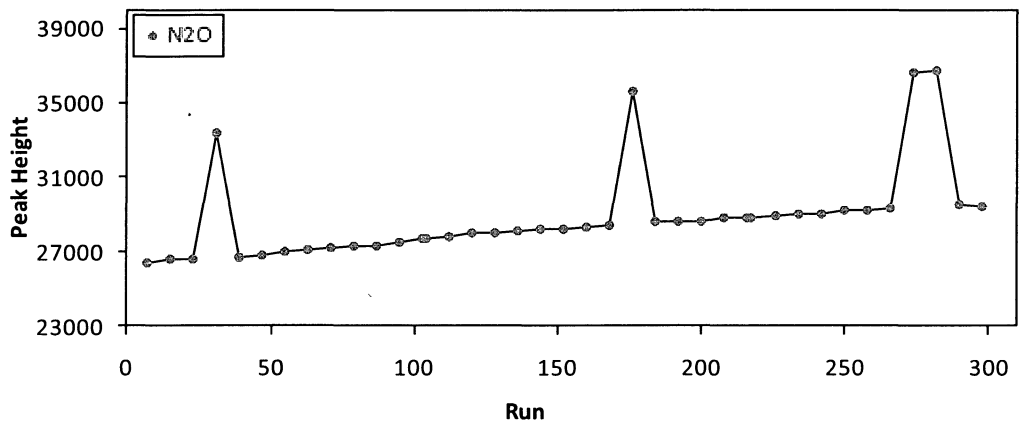

Figure 34. Sampling inconsistency observed during GHGSTD method analysis for nitrous oxide.

As described previously, this problem was resolved by modifying the GHGSTD method by increasing the time intervals between switching of the SSV. Also, an external heater column enclosure (Valco Instruments Co. Inc., Houston, Texas) was added to the system for the molecular sieve 13X analytical column. The enclosure temperature was maintained at 40°C to sharpen the chromatographic peak for carbon monoxide to improve the precision. In addition to the method modifications and the addition of the separate heated column enclosure, the peak height was used for quantification rather than peak area, as this greatly improved the measurement precision.

The measurement precision of the system was evaluated again over a several day period (December 23-26, 2010) using the modified methods listed in Table 13, and the results are displayed in Table 14. It is clear that overall high measurement precision was achieved for each of the gases from the GHGSTD by incorporating these changes; all gases having a relative standard deviation of <1.00%. These results provide confidence in both the calibration standard and the system's overall performance.

3.3.3. Linearity

After the system's precision was optimized, linearity for each gas was evaluated by varying the sample amount. The linearity study was conducted by plotting the peak height as a function of sample amount (i.e., sample loop pressure) for compounds measured with the FID (17.7 to 19.7 psi) and with the ECD (38.7 to 50.7 psi). Figure 35 shows the results of the linearity study for nitrous oxide. Also, Table 15 lists the slope and corresponding uncertainty values for the atmospheric species and the methanizer efficiency obtained during the linearity study.

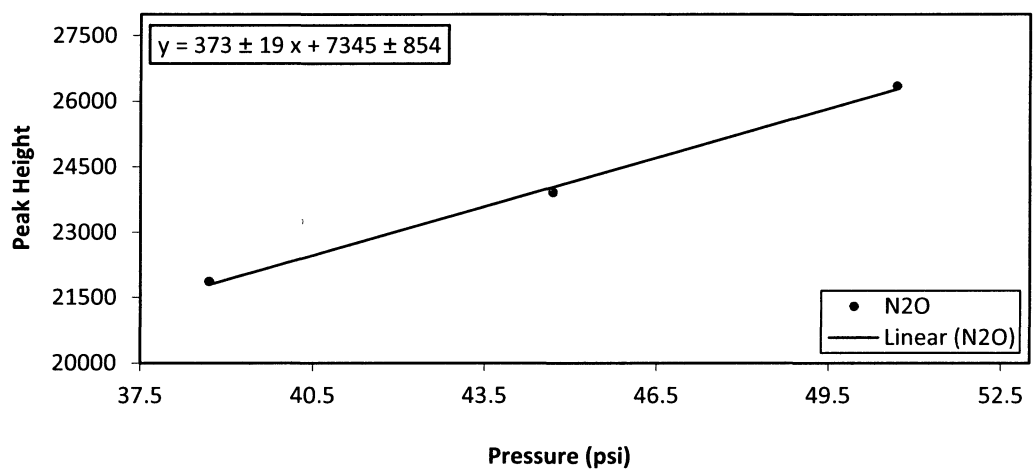

Figure 35. Results of linearity study for nitrous oxide by varying sample loop pressure from 38.7 to 50.7 psi.

Table 15. Slope (m) values acquired during the linear consistency testing.

Atmospheric Species	m
Carbon Monoxide	59.9 ± 0.67
Methane	431 ± 1.25
Carbon Dioxide	42187 ± 279
Nitrous Oxide	373 ± 19.0
Sulfur Hexafluoride	30.0 ± 2.55
Methanizer Efficiency	**m**
Carbon Monoxide/Methane	$6.25 \times 10^{-5} \pm 3.08 \times 10^{-6}$
Carbon Dioxide/Methane	$6.85 \times 10^{-3} \pm 2.74 \times 10^{-4}$

Over the range of values assessed, there is a high linear correspondence for both the FID and ECD detectors. While the range of mixing ratios evaluated covers those observed in the atmosphere, in the future it would be beneficial to conduct the linearity experiments over a wider dynamic range.

3.3.4. Limit of Detection (LOD)

The data acquired from the linearity assessment of the system was further utilized to evaluate the detection limits for each of the gases analyzed. The limit of detection (LOD) was estimated for the FID, with respect to CO, CH_4 and CO_2, and for the ECD, with respect to N_2O and SF_6, using Equation 4,

$$LOD = \frac{(3)(\sigma)}{m} \tag{4}$$

where σ is the standard deviation in the analytical response to standard samples (n = 3) and m is the slope of the calibration curve. The estimated LOD values from Equation 4 are listed in Table 16. The results show that the detection limits are significantly below the observed ambient mixing ratios for the gases of interest, alleviating any issues associated with the integrity of background measurements in the clean, pristine atmosphere.

Table 16. Trace gas limits of detection (LOD) for the GHGGC and typical atmospheric mixing ratios.

Compound	LOD	Typical Atmospheric Mixing Ratios (IPCC 2007)
Carbon Monoxide	2.0 ppbv	90-174 ppbv[a]
Methane	4.5 ppbv	1,774 ppbv
Carbon Dioxide	0.2 ppmv	379 ppmv
Nitrous Oxide	2.5 ppbv	319 ppbv
Sulfur Hexafluoride	1.7 pptv	5.6 pptv

[a][*Pochanart et al.*, 2003]

3.4. Deployment of the Greenhouse Gas GC System

3.4.1. Description of the Field Site

Once the greenhouse gas GC system was quantitatively assessed it was deployed it in the field at the University of New Hampshire's AIRMAP Observing Station at Thompson Farm 2 (TF2) in Durham, NH (43°6'28.61"N, 70°57'6 61"W, elevation 131 ft) (Figure 36). This site is located in a semi-rural environment, 20 km west of the Gulf of Maine and 100 km north of Boston, MA. The location of this site is situated such that it is subject to the influence of both biogenic and anthropogenic emission, making it an ideal site to analyze diverse air masses [e.g., *Cottrell et al* , 2008].

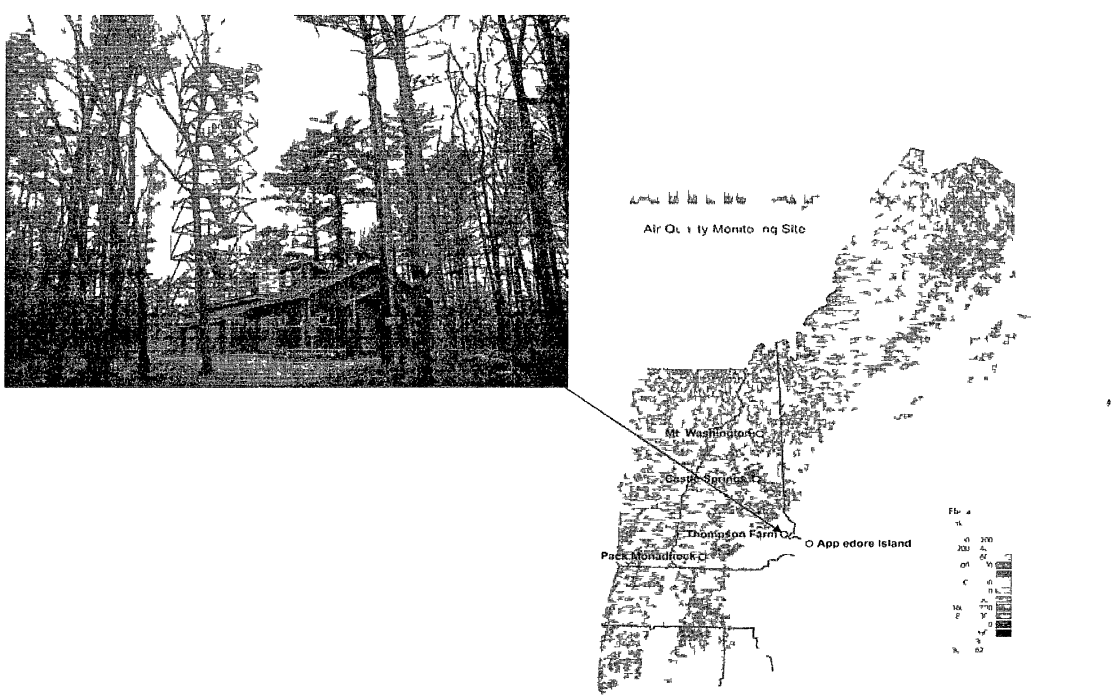

Figure 36. Photo of Thompson Farm 2 and geographic location of the site in eastern New England.

TF2 has a 40 m instrumented sampling tower (Figure 36). Ambient air is continuously drawn from the top of the tower through a 10.2 cm OD Teflon®-coated aluminum

manifold at 1000 L min^{-1} [*Cottrell et al.*, 2008]. The GHGGC samples a sub-stream of ambient air from the manifold for its measurements. Continuous measurements of CO_2, CH_4, N_2O, SF_6 and CO were obtained at TF2 between 6 January and 15 February 2011 as a final validation test of the overall system performance.

3.4.2. Results and Data Analysis

3.4.2.1. ECD Detector Drift

The electron capture detector is prone to long-term drift in the instrument response. In an attempt to correct for this instrument drift and improve the precision of the measurements taken with the greenhouse gas GC system, the data acquired were de-trended using a 2nd order polynomial fit to the raw data (Figure 37). This ultimately resulted in de-trended mixing ratios of sulfur hexafluoride and nitrous oxide.

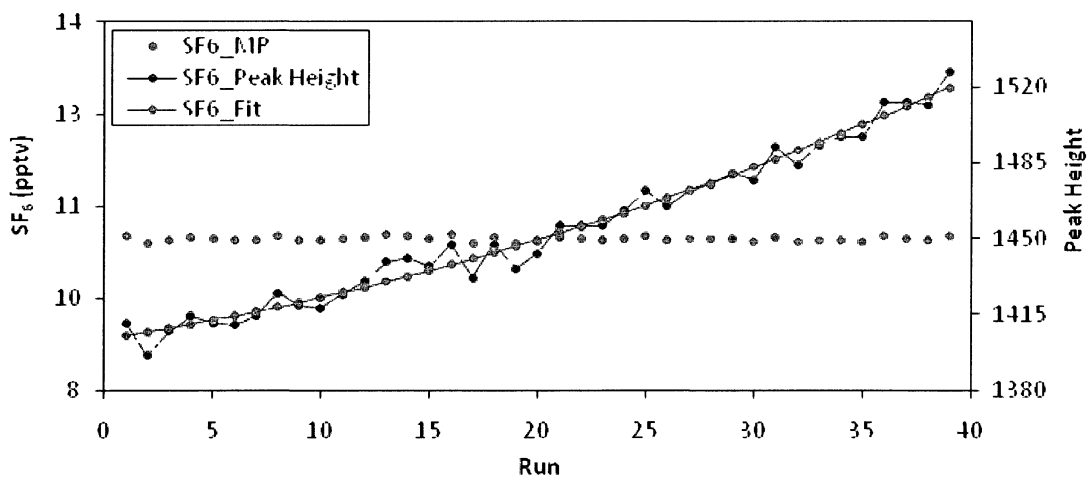

Figure 37. De-trending of the sulfur hexafluoride measurements obtained with the ECD. A polynomial fit was applied to the data for the de-trending process.

3.4.2.2. Ambient Air Measurements

3.4.2.2.1. FID Measurements

The time series plots of CO, CH_4, and CO_2 for the GHGGC at Thompson Farm 2, from 6 January to 15 February 2011, are presented in Figure 38.

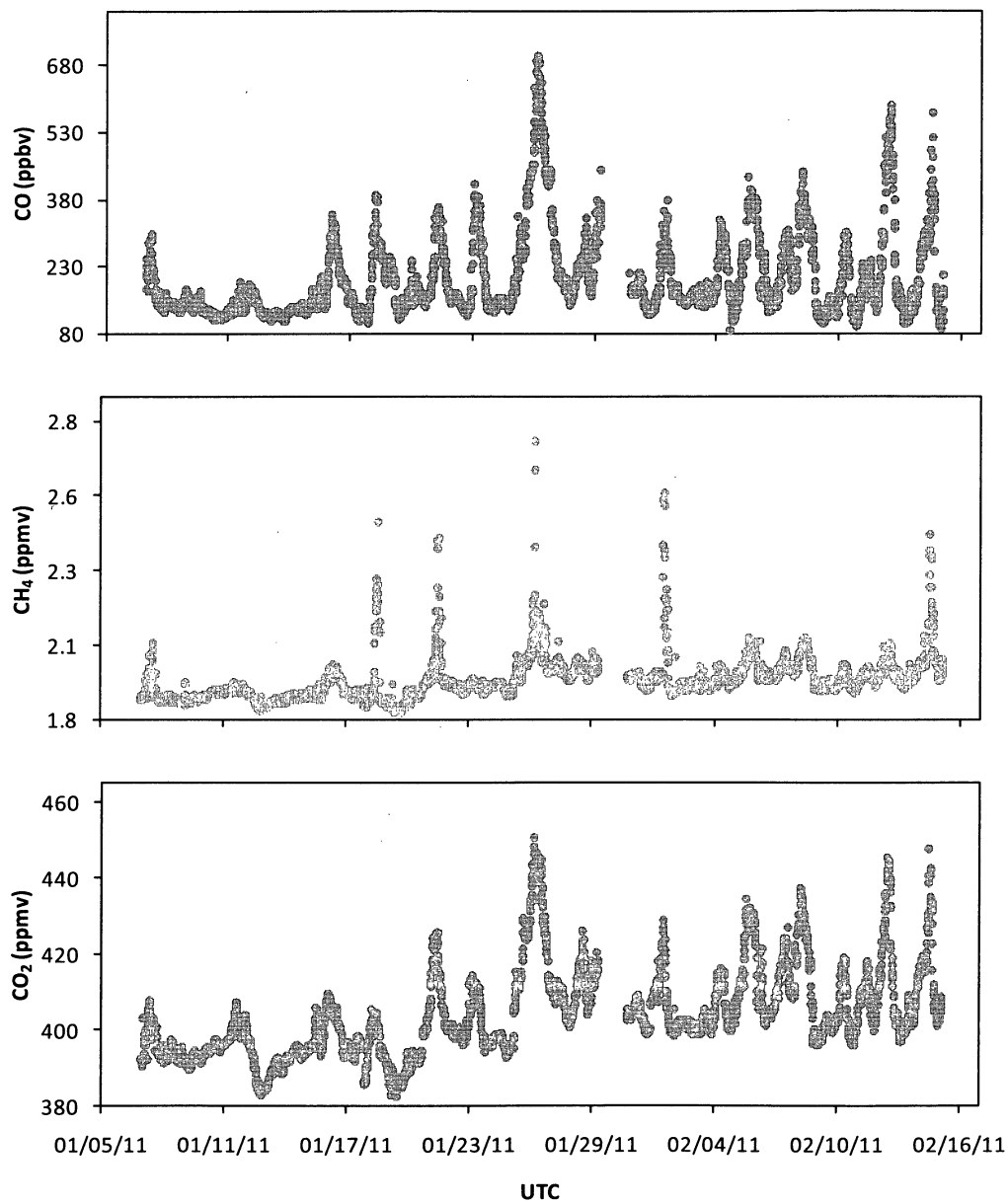

Figure 38. Time series plots of CO, CH_4 and CO_2 for the GHGGC at Thompson Farm 2 from 6 January to 15 February 2011.

Each of the species has significant diurnal and temporal variability throughout this time period. Elevated levels are observed on several occasions. In these CH_4 and CO_2 track well with the criteria pollutant, CO. Overlaid time series plots of these data are displayed in Figure 39.

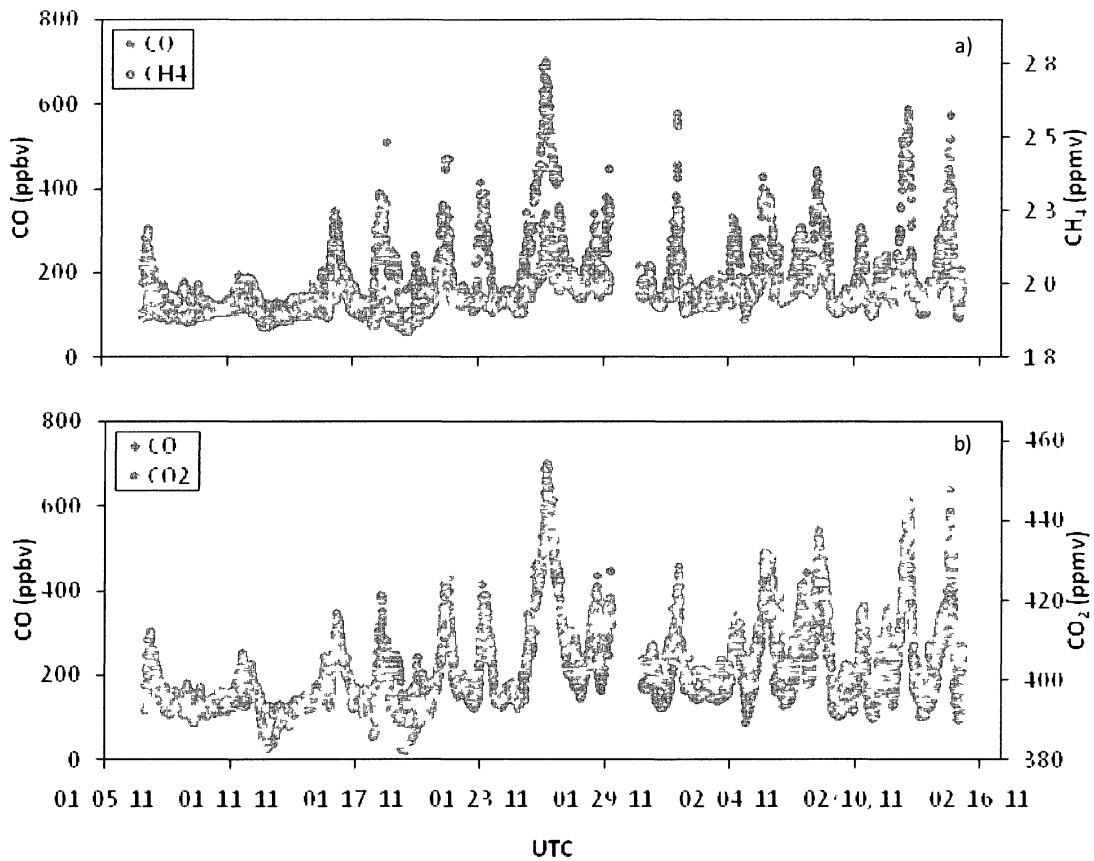

Figure 39. Time series plots of a) CO and CH_4 and b) CO and CO_2 for the GHGGC at Thompson Farm 2 from 6 January to 15 February 2011.

It is apparent that CH_4 and CO track well periodically. This is suggestive of both anthropogenic and biogenic sources of CH_4 during this time period. In contrast to CH_4, the CO and CO_2 data also track very well this is indicative of anthropogenic sources of CO_2. Furthermore, the correlation of CO_2 with CO illustrates that they have similar and/or co-located anthropogenic sources (Figure 40).

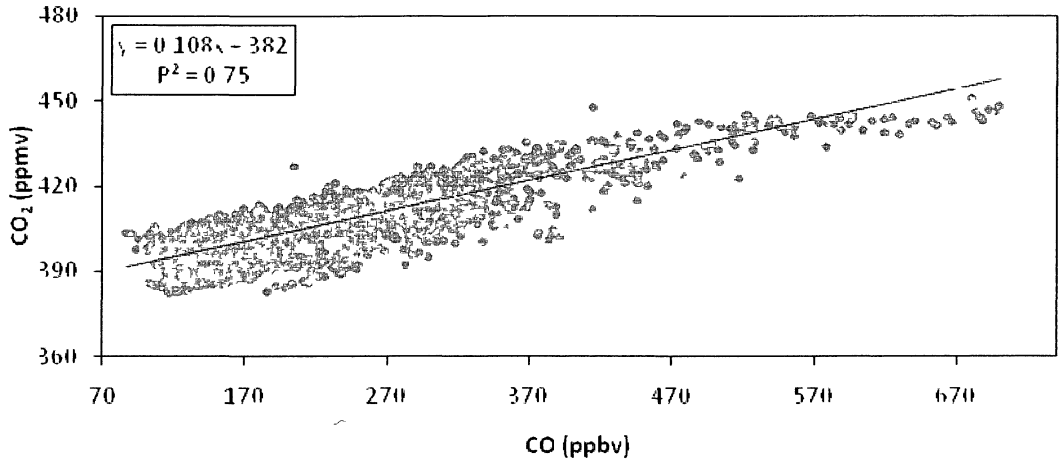

Figure 40. Correlation of CO_2 and CO at Thompson Farm 2 from 6 January to 15 February 2011.

Figure 39 also reveals a sizeable pollution event for CO, CH_4 and CO_2, resulting in increased levels during January 24-27, with maximum mixing ratios occurring on January 26, 2011. This event yielded the highest mixing ratios observed for CO (700 ppbv), CH_4 (2.75 ppmv) and CO_2 (451 ppmv) throughout the entire duration of the instrument deployment. It appears that the CH_4 event originates from of both anthropogenic and biogenic sources as a weak positive correlation is present with CO in the data obtained during the plume (Figure 41). However, a strong positive correlation is also present for CO_2 and CO during the event (Figure 41), suggesting biomass burning and/or fossil fuel combustion as the dominant sources.

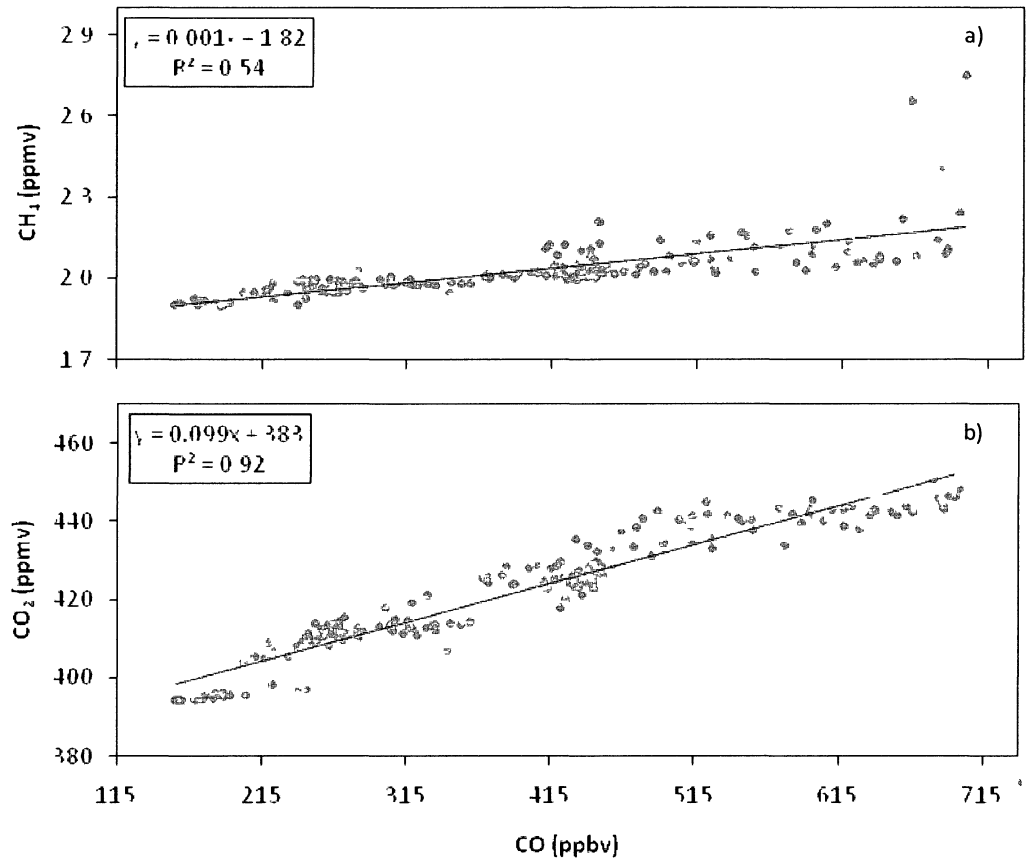

Figure 41. Correlation of a) CH_4 and CO and b) CO_2 and CO at Thompson Farm 2 during a pollution event on 26 January 2011.

In an attempt to further characterize this event the CO data was compared to ancillary measurements of sulfur dioxide (SO_2), nitric oxide (NO) and ozone O_3, which are measured on site at TF2 [www.airmap.unh.edu]. Primary sources of SO_2 and NO include emission from fossil fuel combustion and reaction of N_2 and O_2 in air during high temperature combustion processes, respectively [*Finlayson-Pitts and Pitts*, 2000]. Additionally, O_3, a relatively short lived species as its atmospheric lifetime is on the order of 1 week, is a good indicator of local emissions as production and loss rates are highly dependent on the local chemical environment [*Allen et al.*, 2011]. The instrumentation used for sulfur dioxide measurements consists of a Thermo Environmental Instruments

Model 43C Enhanced Trace Level SO_2 Analyzer (TEI-43C-TLE). The Model 43C-TLE couples pulsed fluorescence technique with a reflective optic design to measure SO_2 at trace levels [*Thermo Environmental Instruments*, 2003]. The instrumentation used for nitric oxide measurements consists of a Thermo Environmental Instruments Model 42C Enhanced Trace Level NO Analyzer (TEI-42C-TL). The Model 42C-TL utilizes chemiluminescence as a measurement technique for NO. Lastly, O_3 is measured using a Thermo Environmental Instruments Model 49C O_3 Analyzer (TEI-49C-PS). The Model 49C-PS utilizes UV photometric detection at 254 nm for O_3 measurements.

Time series plots of CO and SO_2 are shown in Figure 42 during the entire instrument deployment time period (bottom panel) and during the time of the pollution event (top panel). It is apparent that elevated levels of SO_2 are present during the time of the event illustrating the presence of co-located fossil fuel and coal fired power plant emissions as sources. Sulfur-containing gases, primarily sulfur dioxide, emitted into the atmosphere also affect the Earth's radiative budget. For instance, once SO_2 is emitted into the atmosphere it can undergo chemical reactions yielding sulfate aerosol particles that further scatter sunlight back to space [*Watson et al.*, 1992]. SO_2 emissions can also lead to a decreased actinic flux owing to UV absorption by SO_2 (290-330 nm). This can lead to decreases in hydroxyl radical concentrations, ultimately increasing CH_4 and CO growth rates [*Dlugokencky et al.*, 1996].

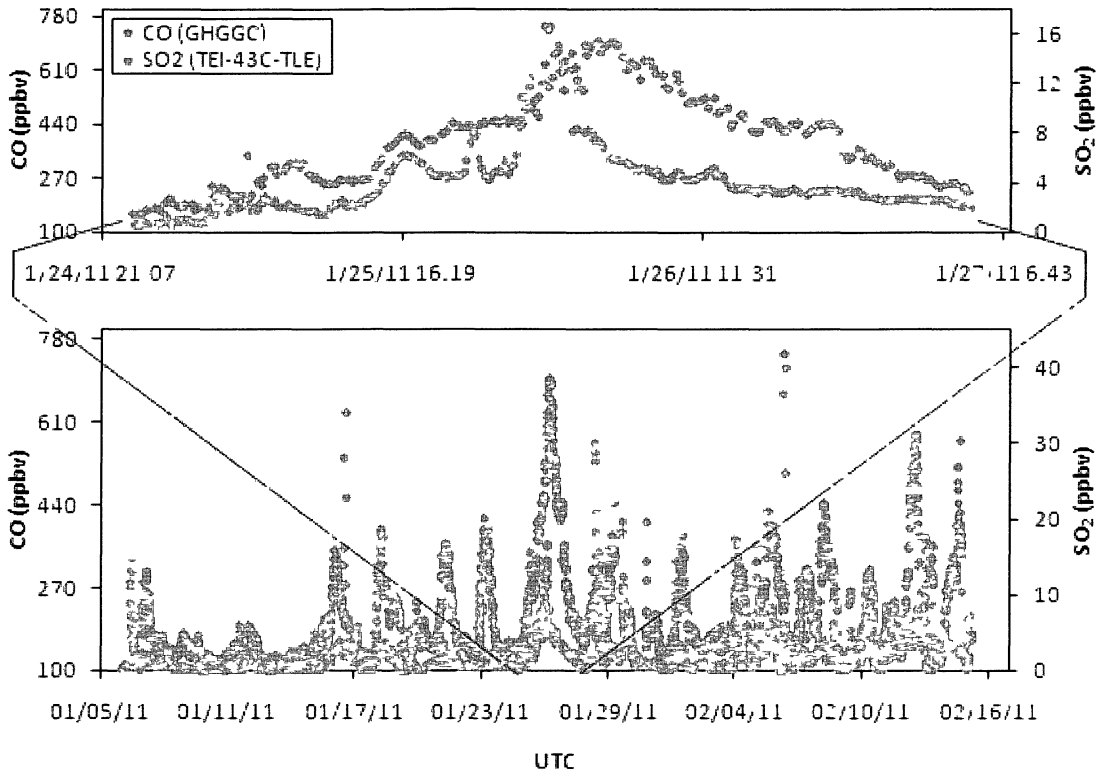

Figure 42. Time series of CO and SO_2 for the duration of the deployment period (bottom panel) and during the January 26 event (top panel).

Time series plots of CO and NO are shown in Figure 43 throughout the instrument deployment (bottom panel) and during the time of the pollution event (top panel). NO mixing ratios are relatively low prior to the event on January 26, 2011, in which they increase significantly. However, in contrast to the CO data, strong diurnal cycling in the NO mixing ratios is present. This feature in the NO data signifies the existence of chemical cycling with its counterpart, nitrogen dioxide (NO_2), and ultimate fate of conversion to nitric acid (HNO_3) [*Brown et al.*, 2004].

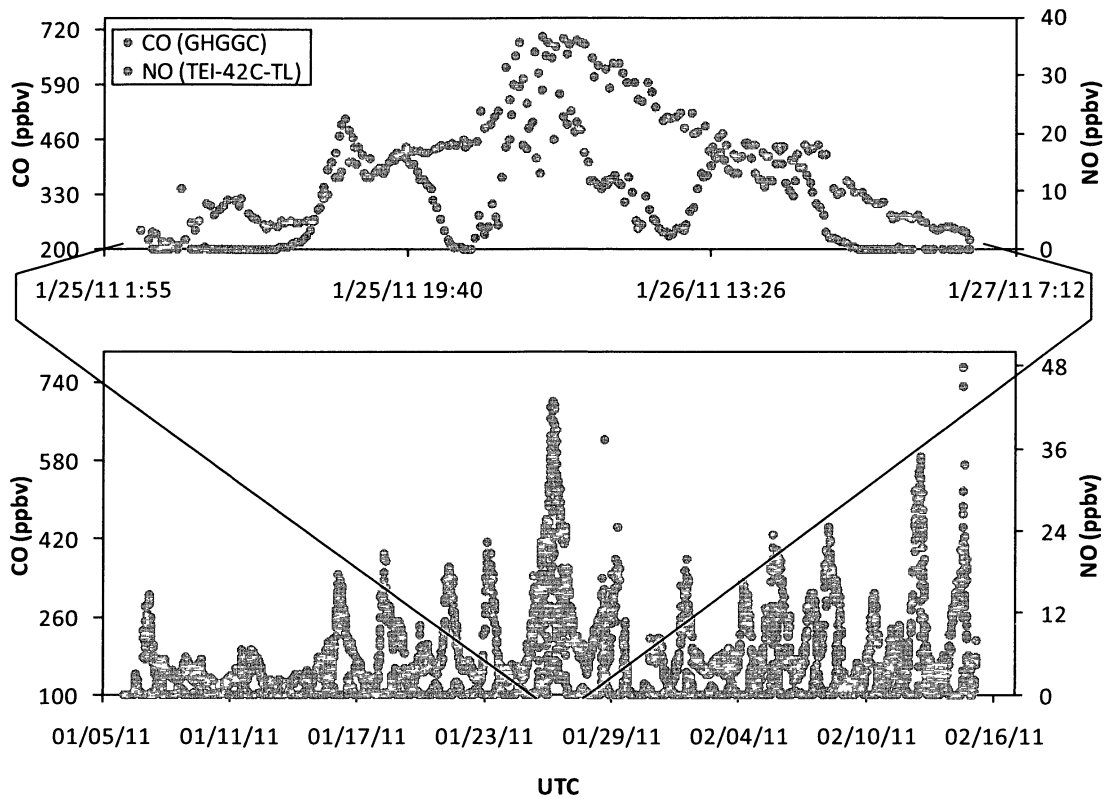

Figure 43. Time series of CO and NO for the duration of the deployment period (bottom panel) and during the January 26 event (top panel).

Moreover, since there is chemical cycling between NO and NO_2, it is typical to report them as a group collectively called nitrogen oxides (NO_x), $NO_x = NO + NO_2$. However, because NO_2 measurements were not available at TF2, only NO is reported here. As previously noted, NO_x exhibits a strong diurnal pattern because it is primarily removed during the nighttime as a result of conversion of NO_2 to nitric acid (HNO_3) [*Brown et al.*, 2004]. Moreover, the removal of NO_2 ultimately results in a loss of NO because of the cycling between the nitrogen oxides. This is clearly illustrated by the pronounced variability in Figure 43. Excluding the strong diurnal cycling in the NO mixing ratios, it is evident that CO and NO correlate well during the event. The atmospheric lifetime of NO_x in the lower atmosphere is on the order of 1 day [*McElroy*, 2002], suggesting the

presence of air parcels from relatively recent combustion emissions on a local or regional scale.

An overlay of CO and O_3 mixing ratios observed during the event is shown in Figure 44. It is evident that CO and O_3 are anti-correlated; this illustrates the presence of local pollution sources building up under a stable nocturnal inversion layer and the subsequent depletion of O_3 by surface deposition or chemical reactions [*Goldstein et al.*, 2004; *Talbot et al.*, 2005]

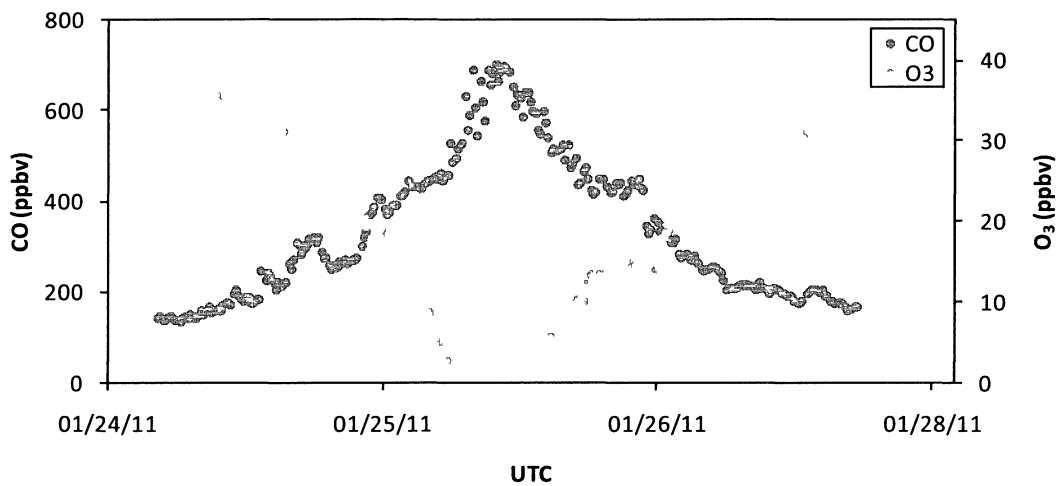

Figure 44. Time series of CO and O_3 for during the 26 January pollution event.

A correlation plot of O_3 as a function of CO is shown in Figure 45 for this event. The correlation plot was generated using data prior to O_3 measurements reaching a minimum (January 24-25, 2011). The strong negative correlation confirms the buildup of emissions from various sources and the persistence of a stable nocturnal boundary layer (e.g., Figure 47) through which ozone can be depleted to very low levels (<10 ppbv) by the combined effects of dry deposition and titration by NO released from mobile sources (Figure 43) [*Talbot et al.*, 2005].

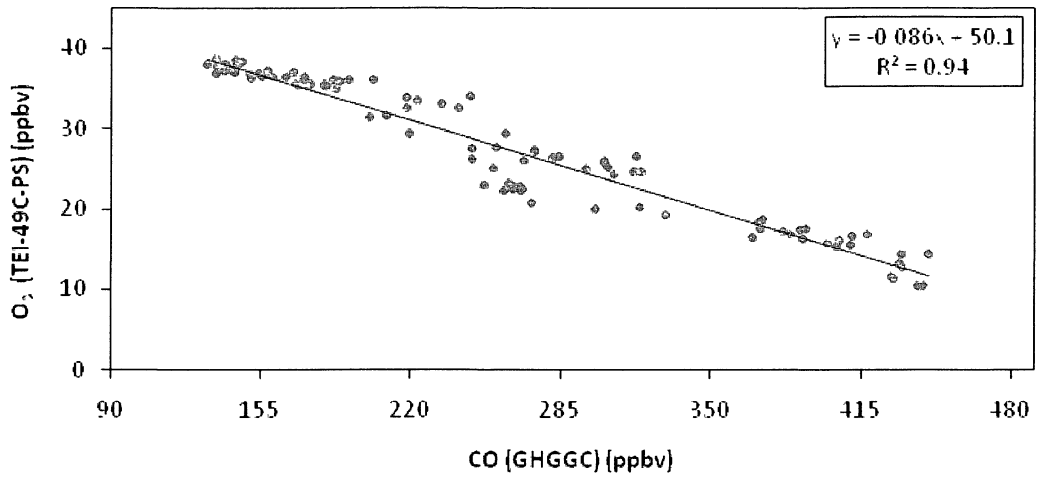

Figure 45. Correlation plot of O_3 as a function of CO during the beginning of the pollution event on January 24-25, 2011.

3.4.2.2.2. ECD Measurements

The time series plots of N_2O and SF_6 for the GHGGC at Thompson Farm 2, from 6 January to 15 February 2011, are presented in Figure 46. The N_2O data had little variability beyond the scope of the background mixing ratios and lacked the appearance of any significant events. Consequently, a four hour period moving average was applied to the data to highlight the underlying trend. However, no apparent diurnal or temporal trend was observed. Conversely, several events were observed in the SF_6 time series plot.

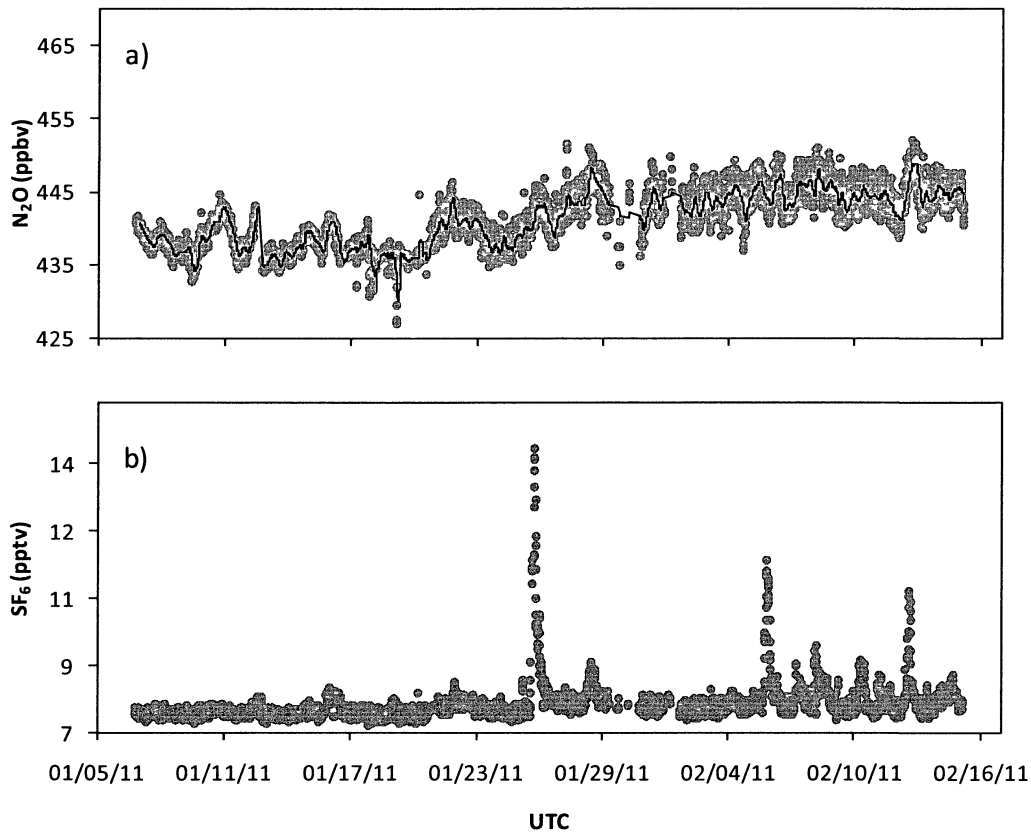

Figure 46. Time series plots of a) N_2O and b) SF_6 for the GHGGC at Thompson Farm 2 from 6 January to 15 February 2011. For N_2O, a four hour period moving average has been included for clarity.

The most significant event occurred on 25 January 2011, less than 24 hours prior to the pollution event observed with the FID channel. During this event, SF_6 mixing ratios reached 14.7 pptv, which is approximately double the average mixing ratio observed throughout the entire instrument deployment. This further suggests that the polluted air mass observed at TF2 contained emissions arising from electrical transmission or distribution as well as combustion emissions. Further investigation of SF_6 is warranted, as is the investigation of the associated events to better understand the sources and distributions in the region.

3.4.2.2.3. Metrological Measurements and Air Mass Transport

In order to understand the general transport pathways and stability of this air mass, wind direction and wind speed data were also analyzed. During the time frame of the event the wind direction was mostly (>90%) composed of westerly to northerly (270°-360°) and southerly to westerly (180°-270°) wind with sporadic (<10%) easterly to southerly (90°-180°) and northerly to easterly (0°-90°) wind (Figure 47). Figure 47 also reveals stable air conditions as wind speeds drop to mean zero during the pollution event.

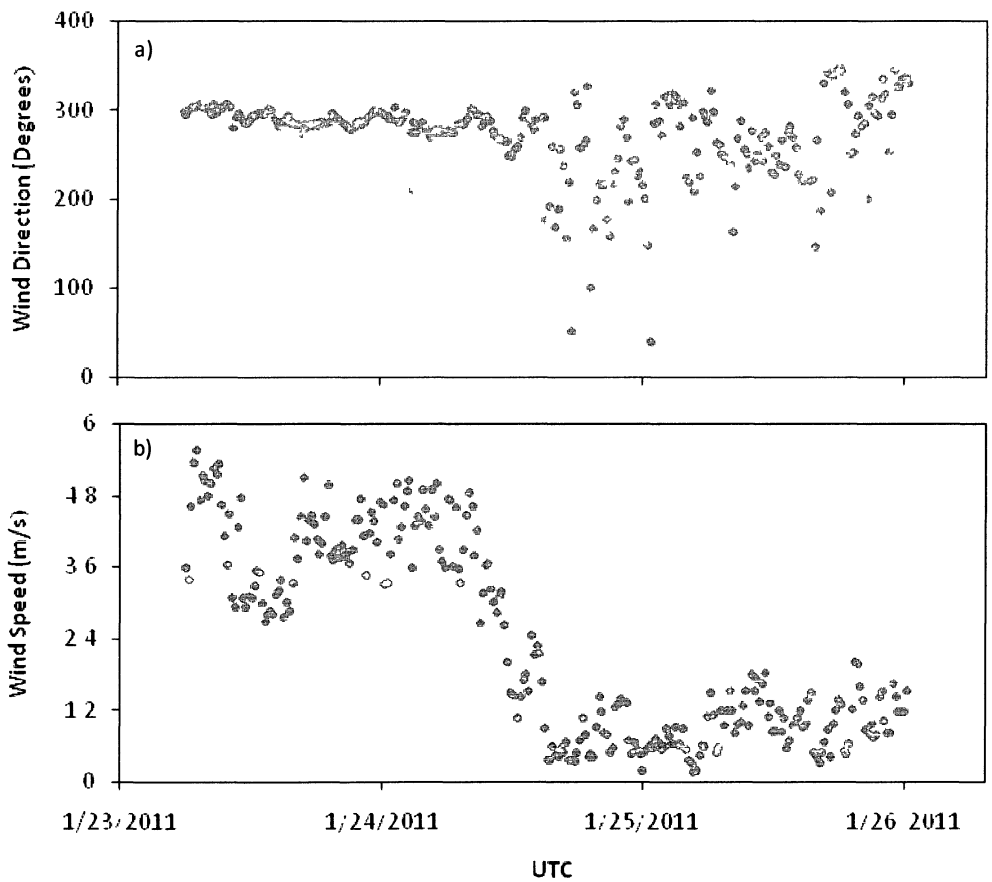

Figure 47. Wind direction (a) and wind speed (b) measured at Thompson Farm 2 during the pollution event.

3.4.2.3. Cross-Validation of CO and CO_2 Measurements

To demonstrate the capabilities of the GHGGC analytical system and to ensure that the quantitative results are in fact reliable the ambient air measurements of CO and CO_2 were compared to those obtained with two infrared based analyzers. The analyzer used for CO measurements was a Thermo Environmental Instruments Model 48C Trace Level CO Analyzer (TEI-48C-TLE). This instrument uses a filter correlation method based on absorption of infrared radiation at 4.6 μm [e.g., *Mao and Talbot*, 2004]. The analyzer used for CO_2 measurements consists of a Li-Cor Biogeosciences Model Li-7000 differential, non-dispersive, infrared (NDIR) gas analyzer.

A time series plot of CO atmospheric mixing ratios as determined using the GHGGC and the TEI-48C-TLE instruments is presented in Figure 48. Overall, the measurements track each other very well, except in a few cases in which higher mixing ratios are observed with the GHGGC, e.g. January 26, 2011.

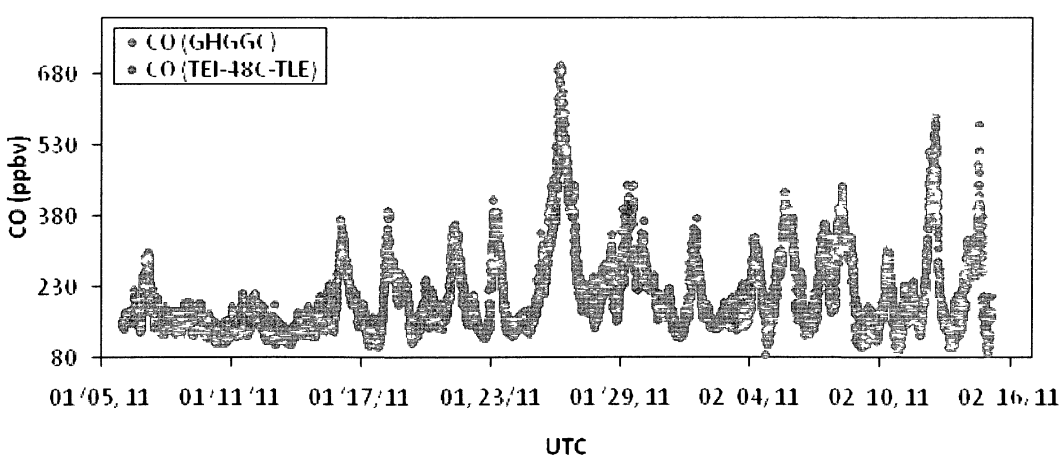

Figure 48. Time series plot of carbon monoxide for the GHGGC and the Thermo Environmental Instruments 48C-TLE analyzer at Thompson Farm 2 from January 6 to February 15, 2011.

A correlation plot of the two different measurement techniques was used to further assess the existing correspondence of the data (Figure 49). Overall, a positive linear correlation exists between the two instruments with a slight negative bias of ~16% observed in the TEI-48C-TLE measurements. It is apparent that the measurements deviate from 1:1 at higher concentrations. The frequency of the CO measurements from the TEI-48C-TLE was 40% lower than that of the GHGGC measurements because of the need to frequently zero and calibrate the instrument because this instrument/technique is highly prone to drift. It is likely that a stronger correlation would exist if more data were available for equivalent analysis times with the two systems.

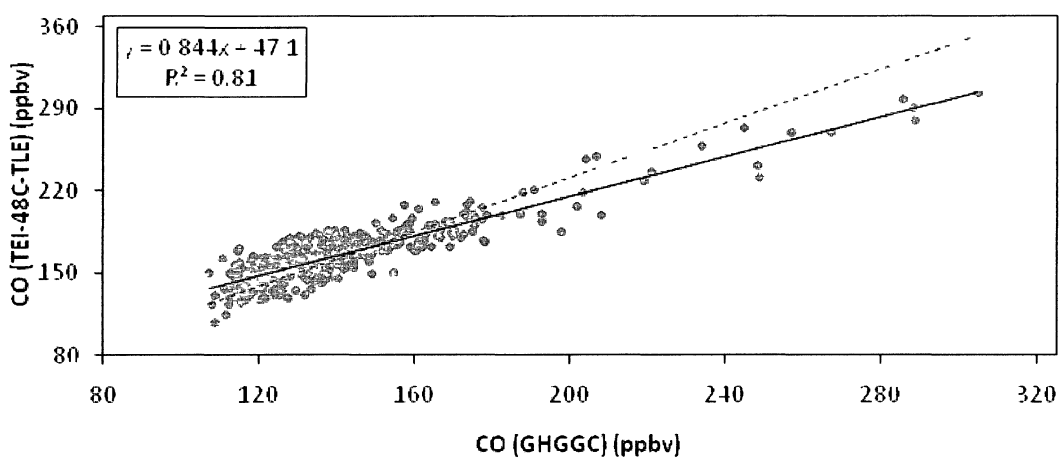

Figure 49. Correlation plot of CO measurements from the Thermo Environmental Instruments 48C-TLE analyzer as a function of CO measurements from the GHGGC at Thompson Farm 2 from January 6 to February 15, 2011. The solid trend line is the regression line and dashed trend line is the 1:1 line.

Table 17 further shows a quantitative comparison of the GHGGC and TEI-48C-TLE CO measurements. The results confirm that overall the two instruments are in good quantitative agreement. However, it is clear that the GHGGC measured higher, high mixing ratios and lower, low lowing ratios than the TEI-48C-TLE analyzer. Additionally,

both systems were calibrated completely independently, providing confidence in both sets of quantitative standards.

Table 17. Quantitative comparison of GHGGC with TEI-48C-TLE and Li-7000 CO and CO_2 measurements.

	CO (GHGGC)	CO (TEI-48C-TLE)	CO_2 (GHGGC)	CO_2 (Li-7000)
Mean	204 ppbv	216 ppbv	404 ppmv	421 ppmv
Median	167 ppbv	189 ppbv	402 ppmv	616 ppmv
Standard Deviation	94 9	75 5	11 8	10 9
Min	87 ppbv	108 ppbv	382 ppmv	410 ppmv
Max	700 ppbv	579 ppbv	451 ppmv	459 ppmv

A time series plot of CO_2 atmospheric mixing ratios as determined using the GHGGC and the Li-Cor is shown in Figure 50. It is apparent that the data track well, although the absolute mixing ratios deviate significantly from one another. Again, both instruments were calibrated independently, and in this case, it is clear there is a significant deviation quantitatively. In this case, because the Li-Cor had been off-line for an extended period of time because of instrument problems, we are not confident in its quantitative results. Additionally, the GHGGC background levels are more in line with those typically observed in this region during this time of year.

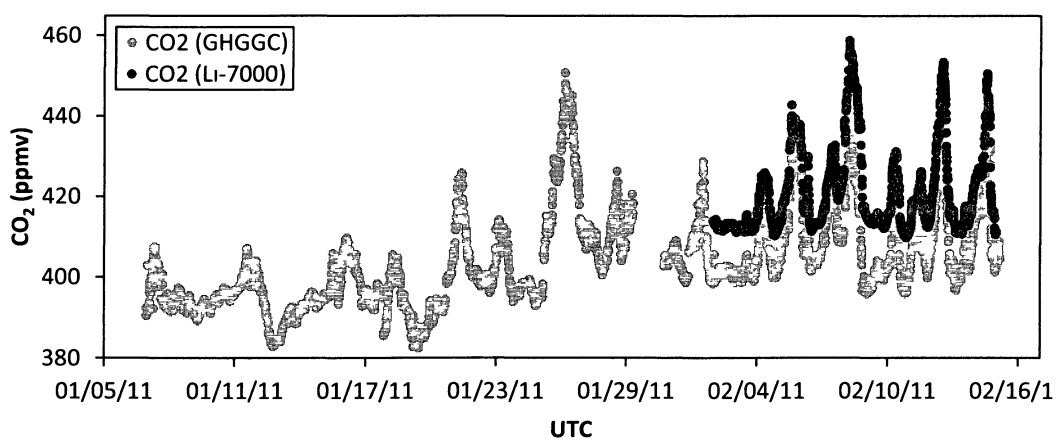

Figure 50. Time series plot of carbon dioxide for the GHGGC and the Li-Cor analyzer at Thompson Farm 2 from January 6 to February 15, 2011.

A correlation plot of CO_2 measurements from the Li-Cor analyzer as a function of CO_2 measurements from the GHGGC is shown in Figure 51 (Note: Li-Cor data from 8 February 2011 was omitted as a result of discrepancies between the two instruments).

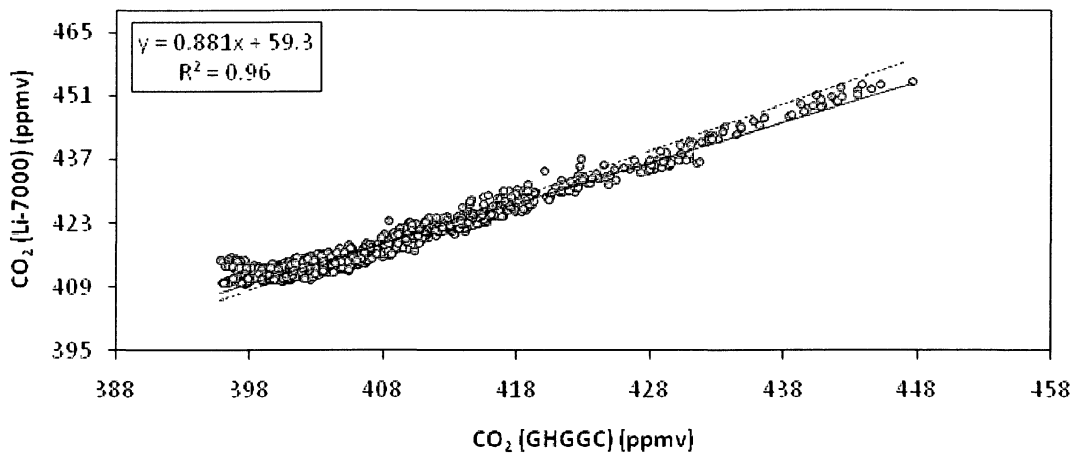

Figure 51. Correlation plot of CO_2 measurements from the Li-Cor analyzer as a function of CO_2 measurements from the GHGGC at Thompson Farm 2 from February 2 to February 15, 2011. The solid trend line is the regression line and dashed trend line is the 1:1 line.

Overall a positive linear correlation exists between the two instruments with a slight negative bias of ~12% observed in the Li-Cor measurements. Table 17 further shows a quantitative comparison of the GHGGC and Li-7000 CO_2 measurements. These results clarify the deviations observed in the time series plots and corroborate the quantitative discrepancy between the two systems. Although lower mixing ratios were observed with GHGGC, the magnitude of variation in the measurements was comparable between the two systems. Even though we are not confident in the quantitative results obtained with the Li-Cor instrument, the existing correspondence of the data provides confidence in the qualitative results.

3.5. Summary

The greenhouse gas GC system has been rigorously characterized both in the laboratory and in the field. Results from the ambient analyses of CO_2, CH_4, N_2O, SF_6 and CO provide confidence in the methanizer efficiency, calibration standards and the system's overall performance. Furthermore, a comparison of ambient results to ancillary measurements (e.g., SO_2, NO, O_3, CO and CO_2) ensures the quality of the analytical result.

CHAPTER 4

CONCLUSIONS

High-precision, continuous monitoring of greenhouse gases, such as carbon dioxide (CO_2), methane (CH_4), nitrous oxide (N_2O), sulfur hexafluoride (SF_6), and the criteria pollutant carbon monoxide (CO), is important for characterizing their regional sources and sinks and understanding how their ambient levels are changing with time and anthropogenic activities. For monitoring this suite of gases, we have built a fully automated gas chromatographic-based analytical system and deployed it in the field at the UNH AIRMAP Observing Station at Thompson Farm in Durham, NH. The instrument consists of a Shimadzu 17A gas chromatograph (GC), equipped with a Flame Ionization Detector (FID) and a custom-built methanizer for the measurements of CO_2, CH_4 and CO; additionally, the GC is equipped with an Electron Capture Detector (ECD) used for measurements of N_2O and SF_6.

The performance of the system has been assessed and it is apparent that a high linear correspondence exists; confirming the linearity of the FID and ECD detectors, analytical system, and also the accuracy of pressurizing the sample loops. Furthermore, these results provide confidence in the methanizer efficiency, calibration standard and the system's overall performance.

Results from the ambient analyses of CO_2, CH_4, N_2O, SF_6 and CO revealed a pollution event at TF2 whose composition was consistent with emissions from electrical transmission or distribution as well as local combustion emissions.

Finally, a comparison of the gas chromatographic based ambient analyses of CO and CO_2 with infrared-based analyzers confirms the quality of the analytical result. Overall, the GHGGC and TEI CO measurements were in good quantitative agreement and the two systems tracked each other well. The GHGGC and Li-Cor measurements were in good qualitative agreement; the two systems also tracked each other well.

LIST OF REFERENCES

Allen, G. et al. (2011), Southeast Pacific atmospheric composition and variability sampled along 20◦ S during VOCALS-REx, *Atmos. Chem. Phys. Discuss.*, 11, 681–744, doi:10.5194/acpd-11-681-2011.

Arrhenius S. (1896), On the Influence of Carbonic Acid in the Air upon the Temperature of the Ground, *Philosophical Magazine and Journal of Science* **41**, 237–275.

Brasseur, G. et al. (1999), *Atmospheric chemistry and global change*. Oxford University Press, Oxford, New York.

Brown, S. S. et al. (2004), Nighttime removal of NO_x in the summer marine boundary layer, Geophys. Res. Lett., 31, L07108, doi:10.1029/2004GL019412.

Berner, E.K. and R.A. Berner (1996), *Global Environment: Water, Air and Geochemical Cycles*. Prentice-Hall, Upper Saddle River, NJ.

Cockerham, L., and B. Shane (1994), *Basic Environmental Toxicology*, CRC Press, Inc., USA.

Conway, T.J. et al. (1988), Atmospheric carbon dioxide measurements in the remote global troposphere, 1981-1984, *Tellus, 40B, 81-115.*

Cottrell, L. D. et al. (2008), Submicron particles at Thompson Farm during ICARTT measured using aerosol mass spectrometry, *J. Geophys. Res.-Atmos.*, 113, D08212, doi:10.1029/2007JD009192.

Crouch, S., J. Holler, D. Skoog (1998), *Principles of Instrumental Analysis*, 6th ed., Thomson Brooks/Cole, Belmont, CA.

Dlugokencky, E. et al. (1994), The growth rate and distribution of atmospheric methane, *J. Geophys. Res.* 99, 17021–17043.

Dlugokencky, E. et al. (1996), Changes in CH_4 and CO growth rates after the eruption of Mt. Pinatubo and their link with changes in tropical tropospheric UV flux. *Geophys. Res. Lett.*, 23(20), 2761–2764.

Dlugokencky, E. et al. (1997), Is the amplitude of the methane seasonal cycle changing? *Atmos. Environ.* 31, 21– 26.

Finlayson-Pitts, B. J.; Pitts, J. N., Jr. *Chemistry of the Upper and Lower Atmosphere*; Academic Press: San Diego, CA, 2000.

Forster, P. et al. (2007), Changes in Atmospheric Constituents and in Radiative Forcing. *In: Climate Change 2007: The Physical Science Basis. Contribution of Working Group I to the Fourth Assessment Report of the Intergovernmental Panel on*

Climate Change [Solomon, S. et al. (eds.)]. Cambridge University Press, Cambridge, United Kingdom and New York, NY, USA.

Forsyth, D. S. (2004), *Journal of Chromatography A* **1050**, 63–68.

Geller, L. S. et al. (1997), Tropospheric SF_6: Observed latitudinal distribution and trends, derived emissions, and interhemispheric exchange time, *Geophys. Res. Lett.*, 24, 675–678.

Goldstein, A. H. et al. (2004), Impact of Asian emissions on observations at Trinidad Head, California, during ITCT 2K2, *J. Geophys. Res.*, 109, D23S17, doi:10.1029/2003JD004406.

Griffin, R. J. et al. (2004), Quantification of ozone formation metrics at Thompson Farm during NEAQS 2002, *J. Geophys. Res.*, 109, D24302, doi:10.1029/2004JD005344.

Grob, R., and E. Barry (1995), *Modern Practice of Gas Chromatography*, Wiley, New York.

Habazaki, H. et al. (1998), Applied Catalysis A: General 172, 131-140.

Haberhauer-Troyer, C., E. Rosenberg and M. Grasserbauer (1999), *Journal of Chromatography A*, 852, 589–595.

Hart, A. B.S. Thesis, University of New Hampshire, Durham, 2009.

Jacob, D. (1999), *Introduction to Atmospheric Chemistry*. Princeton, NJ: Princeton Univ. Press.

Karbiwnyk, C.M. et al. (2002), *Journal of Chromatography A*, 958, 219-229.

Kozlova, E. A. and Manning, A. C.: Methodology and calibration for continuous measurements of biogeochemical trace gas and O_2 concentrations from a 300-m tall tower in central Siberia, *Atmos. Meas. Tech.*, 2, 205–220.

Leckrone, K. J., and J.M. Hayes (1997), *Anal. Chem.* 69, 911–918.

Le Treut, H. et al. (2007), Historical Overview of Climate Change. *In: Climate Change 2007: The Physical Science Basis. Contribution of Working Group I to the Fourth Assessment Report of the Intergovernmental Panel on Climate Change* [Solomon, S. et al. (eds.)]. Cambridge University Press, Cambridge, United Kingdom and New York, NY, USA.

Manning, A. C., and R. F. Keeling (2006), Global oceanic and land biotic carbon sinks from the Scripps atmospheric oxygen flask sampling network. *Tellus,* **58B,** 95–116.

McNair, H. and E. Bonelli (1969), *Basic Gas Chromatography*, Varian Aerography, Palo Alto, CA.

Mao, H., and R. Talbot (2004), O3 and CO in New England: Temporal variations and relationships, *J. Geophys. Res.*, 109, D21304, doi:10.1029/2004JD004913.

McElroy, M. B. (2002), *The Atmospheric Environment: Effects of Human Activity*, Princeton Univ. Press, Princeton, N.J.

Nevison, C. D., D. E. Kinnison and R. F. Weiss (2004), Stratospheric influence on the tropospheric seasonal cycles of nitrous oxide and chlorofluorocarbons, *Geophys. Res. Lett.*, 31, L20103, doi:10.1029/2004GL020398.

Nollet, L. (2006), *Chromatographic Analysis of the Environment*, CRC Press, Boca Ranton, FL.

Patra, P. K. et al. (2009), Transport mechanisms for synoptic, seasonal and interannual SF_6 variations and ''age'' of air in the troposphere, *Atmos. Chem. Phys.*, 9, 1209–1225.

Pochanart, P. et al. (2003), Regional background ozone and carbon monoxide variations in remote Siberia/East Asia, *J. Geophys. Res.*, 108, doi:10.1029/2001JD001412.

Popa, M. E. (2008), Continuous tall tower multi-species measurements in Europe for quantifying and understanding land-atmosphere carbon exchange, PhD. thesis, Friedrich Schiller University, Jena. Available at http://www.db-thueringen.de/servlets/DerivateServlet/Derivate-14971/Popa/Dissertation.pdf, http://www.bgc-jena.mpg.de/bgc-systems/dissertations/Popa thesis.pdf.

Popa, M. E. et al. (2010), Measurements of greenhouse gases and related tracers at Bialystok tall tower station in Poland, *Atmos. Meas. Tech.*, 3, 407–427.

Ramaswamy V., et al. (2001), Radiative forcing of climate change. *In: Climate Change 2001: The Scientific Basis. Contribution of Working Group I to the Third Assessment Report of the Intergovernmental Panel on Climate Change* [Houghton, J.T., et al. (eds.)]. Cambridge University Press, Cambridge, United Kingdom and New York, NY, USA.

Scripps CO2 Program (2010), CO2 Concentration at Mauna Lao Observatory, Hawaii. Scripps Institution of Oceanography, University of California, San Diego. Available at http://scrippsco2.ucsd.edu/research/atmospheric_co2.html.

Sigma-Aldrich Co. (2003-2004), Particle Size Conversion, Aldrich 2003-2004 Catalog/Handbook of Fine Chemicals, T848.

Sive, B. C. Ph.D. Dissertation, University of California, Irvine, 1998.

Steele, L. P. et al. (1987), The global distribution of methane in the troposphere, *J. Atmos. Chem.*, *5*, 125–171.

Talbot, R. et al. (2005), Diurnal characteristics of surface level O_3 and other important grace gases in New England, *J. Geophys. Res.*, 110, D09307, doi:10.1029/2004JD005449.

Tans, P. (2010), NOAA/ESRL, available at http://www.esrl.noaa.gov/gmd/ccgg/iadv/.

Thermo Environmental Instruments (2003), Model 43C-TLE Enhanced Trace Level SO_2 Analyzer for Continuous Monitoring. Lit. 43CTLEMC1004.

Thompson, R. et al. (2009), In-situ measurements of oxygen, carbon monoxide and greenhouse gases from Ochsenkopf tall tower in Germany, *Atmos. Meas. Tech. Discuss.*,2, 1247–1291.

Tohjima, Y. et al. (2000), Variations in atmospheric nitrous oxide observed at Hateruma monitoring station, *Chemosphere*, 2, 435–443.

U.S. EPA (2010), *Inventory of U.S. Greenhouse Gas Emissions and Sinks: 1990 - 2008.*

Van der Laan, S. et al. (2009), A single gas chromatograph for atmospheric mixing ratio measurements of CO_2, CH_4, N_2O, SF_6, and CO, *Atmos. Meas. Tech.*, 2, 549-559.

VICI Valco Instruments Co. Inc. (1998), Pulsed Discharge Detector Models D-2 and D-2-I Instruction Manual.

von Rohden C. and J. Ilmberger (2001), Tracer experiment with sulfur hexafluoride to quantify the vertical transport in a meromictic pit lake. *Aquat. Sci.* 63, 417–431.

Watson, R. et al. (1990), Greenhouse gases and aerosols. *In: Climate Change. The IPCC Scientific Assessment.* [Houghton, J.T. et al. (eds.)]. Cambridge University Press, Cambridge, United Kingdom and New York, NY, USA.

Watson, R. et al. (1992), Greenhouse Gases: Sources and Sinks. *In: Climate Change. The Supplementary Report to the IPCC Scientific Assessment.* [Houghton, J.T. et al. (eds.)]. Cambridge University Press, Cambridge, United Kingdom and New York, NY, USA.

Yuwono, M., and G. Indrayanto (2005), Gas Chromatography In: Ewing's Analytical Instrumentation Handbook. USA: Marcel Dekker.